Two opposite voltage-dependent currents control the unusual early development pattern of embryonic Renshaw cell electrical activity

Juliette Boeri, Claude Meunier, Hervé Le Corronc, Pascal Branchereau, Yulia Timofeeva, François-Xavier Lejeune, Christine Mouffle, Hervé Arulkandarajah, Jean Marie Mangin, Pascal Legendre, et al.

Two opposite voltage-dependent currents control the unusual early development pattern of embryonic Renshaw cell electrical activity

Juliette Boeri[1¶], Claude Meunier[2 ¶], Hervé Le Corronc[1,3 ¶], Pascal Branchereau[4], Yulia Timofeeva[5,6], François Xavier Lejeune[7], Christine Mouffle[1], Hervé Arulkandarajah[1], Jean Marie Mangin[1], Pascal Legendre[1&]*, Antonny Czarnecki[1,4&]*

Affiliation

[1] INSERM, UMR_S 1130, CNRS, UMR 8246, Neuroscience Paris Seine, Institute of Biology Paris Seine, Sorbonne Univ, Paris, France.
[2] Centre de Neurosciences Intégratives et Cognition, CNRS UMR 8002, Institut Neurosciences et Cognition, Université de Paris, Paris, France.
[3] Univ Angers, Angers, France.
[4] Univ. Bordeaux, CNRS, EPHE, INCIA, UMR 5287 F-33000 Bordeaux, France
[5] Department of Computer Science and Centre for Complexity Science, University of Warwick, Coventry, UK.
[6] Department of Clinical and Experimental Epilepsy, UCL Queen Square Institute of Neurology, University College London, London, UK.
[7] Institut du Cerveau et de la Moelle Epinière, Centre de Recherche CHU Pitié-Salpétrière, INSERM, U975, CNRS, UMR 7225, Sorbonne Univ, Paris, France.

* Corresponding authors
Email: pascal.legendre@inserm.fr (PL)
Email: antonny.czarnecki@u-bordeaux.fr (AC)

[¶]These authors contributed equally to this work.

[&]These authors also contributed equally to this work.

Abstract

Renshaw cells ($V1^R$) are excitable as soon as they reach their final location next to the spinal motoneurons and are functionally heterogeneous. Using multiple experimental approaches, in combination with biophysical modeling and dynamical systems theory, we analyzed, for the first time, the mechanisms underlying the electrophysiological properties of V1R during early embryonic development of the mouse spinal cord locomotor networks (E11.5-E16.5). We found that these interneurons are subdivided into several functional clusters from E11.5 and then display an unexpected transitory involution process during which they lose their ability to sustain tonic firing. We demonstrated that the essential factor controlling the diversity of the discharge pattern of embryonic $V1^R$ is the ratio of a persistent sodium conductance to a delayed rectifier potassium conductance. Taken together, our results reveal how a simple mechanism, based on the synergy of two voltage-dependent conductances that are ubiquitous in neurons, can produce functional diversity in embryonic $V1^R$ and control their early developmental trajectory.

Keywords: development, spinal cord, embryo, Renshaw cell, firing pattern, functional involution, electrophysiology, biophysical modeling.

Introduction

The development of the central nervous system (CNS) follows complex steps, which depend on genetic and environmental factors and involve interactions between multiple elements of the neural tissue. Remarkably, emergent neurons begin to synchronize soon after the onset of synapse formation, generating long episodes of low frequency (<0.01 Hz) correlated spontaneous network activity (SNA) [1-8]. In the mouse embryonic spinal cord (SC), SNA is driven by an excitatory cholinergic-GABAergic loop between motoneurons (MNs) and interneurons (INs), GABA being depolarizing before embryonic day 16.5 (E16.5) [9]. SNA emerges around E12.5 [4, 6, 10-12], at a time when functional neuromuscular junctions are not yet established [13], and sensory and supraspinal inputs have not yet reached the spinal motor networks [14-17].

Several studies pointed out that SNA is an essential component in neuronal networks formation. [18-21]. In the SC, pharmacologically-induced disturbances of SNA between E12.5 and E14.5 induce defects in the formation of motor pools, in motor axon guidance to their target muscles and in the development of motor networks [4, 21-23]. During SNA episodes, long lasting giant depolarization potentials (GDPs) are evoked in the SC, mainly by the massive release of GABA onto MNs [12]. Immature Renshaw cells ($V1^R$) are likely the first GABAergic partners of MNs in the mouse embryo [24, 25], and the massive release of GABA during SNA probably requires that many of them display repetitive action potential firing or plateau potential activity [25].

However, little is known about the firing pattern of embryonic $V1^R$ and the maturation of their intrinsic properties. We recently found that $V1^R$ exhibit heterogeneous excitability properties when SNA emerges in the SC [25] in contrast to adult Renshaw cells that constitute a functionally homogeneous population [26, 27]. Whether this early functional

diversity really reflects distinct functional classes of $V1^R$, how this diversity evolves during development, and what are the underlying biophysical mechanisms remain open questions. The present study addresses these issues using multiple approaches, including patch-clamp recordings, cluster analysis, biophysical modeling and dynamical systems theory. The firing patterns of $V1^R$ and the mechanisms underlying their functional diversity are analyzed during a developmental period covering the initial phase of development of SC activity in the mouse embryo (E11.5-E14.5), when SNA is present, and during the critical period (E14.5-E16.5), when GABAergic neurotransmission gradually shifts from excitation to inhibition [28] and locomotor-like activity emerges [4, 10, 11].

We discover that the balance between the slowly inactivating subthreshold persistent sodium inward current (I_{Nap}) [29] and the delayed rectifier potassium outward current (I_{Kdr}), accounts for the heterogeneity of embryonic $V1^R$ and the changes in firing pattern during development. The heterogeneity of $V1^R$ at E12.5 arises from the existence of distinct functional groups. Surprisingly, and in opposition to the classically accepted development scheme [30-35], we show that the embryonic $V1^R$ population loses its ability to support tonic firing from E13.5 to E15.5, exhibiting a transient functional involution during its development. Our experimental and theoretical results provide a global view of the developmental trajectories of embryonic $V1^R$. They demonstrate that a simple mechanism, based on the synergy of only two major opposing voltage-dependent currents, accounts for functional diversity in these immature neurons.

Results

The delayed rectifier potassium current I_{Kdr} is a key partner of the persistent sodium current I_{Nap} in controlling embryonic $V1^R$ firing patterns during development

We previously highlighted that $V1^R$ are spontaneously active at E12.5. Their response to a 2 s suprathreshold depolarizing current steps revealed four main patterns, depending of the recorded interneuron [25]: i) single spiking (SS) $V1^R$ that fires only 1-3 APs at the onset of the depolarizing pulse, ii) repetitive spiking (RS) $V1^R$, iii) mixed events (ME) $V1^R$ that shows an alternation of action potentials (APs) and plateau potentials or, iv) $V1^R$ that displays a long-lasting sodium-dependent plateau potential (PP) (***Figure 1A1–A4***).

We also uncovered a relationship between I_{Nap} and the ability of embryonic $V1^R$ to sustain repetitive firing [25]. However, the heterogeneous firing patterns of $V1^R$ observed at E12.5 could not be fully explained by variations in I_{Nap} [25], suggesting the involvement of other voltage-gated channels in the control of the firing pattern of $V1^R$, in particular potassium channels, known to control firing and AP repolarization. Our voltage clamp protocol, performed in the presence of TTX (1 μM), did not disclose any inward rectifying current (hyperpolarizing voltage steps to -100 mV from V_H = -20 mV, data not shown), but revealed two voltage-dependent outward potassium currents, a delayed rectifier current (I_{Kdr}) and a transient potassium current (I_A) in all embryonic $V1^R$, whatever the firing pattern (***Figure 1B1–B4***). These currents are known to control AP duration (I_{Kdr}) or firing rate (I_A), respectively [36]. The activation threshold of I_{Kdr} lied between -30 mV and -20 mV and the threshold of I_A between -60 mV and -50 mV, (n = 27; N = 27 embryos) (***Figure 1C1–C4***). Removing external calcium had no effect on potassium current I/V curves (data not shown), suggesting that calcium-dependent potassium currents are not yet present at E12.5.

It was unlikely that the heterogeneity of $V1^R$ firing patterns resulted from variations in the intensity of I_A. Indeed, its voltage-dependent inactivation (time constant: 23.3 ± 2.6 ms, n = 8; N = 8), which occurs during the depolarizing phase of an AP, makes it ineffective to

control AP or plateau potential durations. This was confirmed by our theoretical analysis (***see Figure 7—figure supplement 1***). We thus focused our study on I_{Kdr}. At E12.5, PP V1^R had a significantly lower G_{Kdr} (2.12 ± 0.44 nS, n = 6; N = 6) than SS V1^R (5.57 ± 0.56 nS, n = 9; N = 9) and RS V1^R (6.39 ± 0.83 nS, n = 7; N = 7) (***Figure 1D***). However, there was no significant difference in G_{Kdr} between SS V1^R and RS V1^R at E12.5 (***Figure 1D***), which indicated that variations in G_{Kdr} alone could not explain all the firing patterns observed at E12.5. Similarly, there was no significant difference in G_{Nap} between RS V1^R (0.91 ± 0.21nS, n = 8; N = 8) and PP V1^R (1.24 ± 0.19 nS, n = 6; N = 6) at E12.5 (***Figure 1E***), indicating that variations in G_{Nap} alone could not explain all the firing patterns of V1^R at E12.5 [25]. In contrast G_{Nap} measured in SS V1^R at E12.5 (0.21 ± 0.20 nS, n = 9; N = 9) were significantly lower compared to G_{Nap} measured in RS V1^R and in PP V1^R at E12.5 (***Figure 1E***).

Mature neurons often display multiple stable firing patterns [37-39]. This usually depends on the combination of several outward and inward voltage- or calcium-dependent conductances and on their spatial localization [37-39]. In contrast, immature V1^R have a limited repertoire of voltage-dependent currents (I_{Nat} and I_{Nap}, I_{Kdr} and I_A) at E12.5, and we did not find any evidence of voltage-dependent calcium currents at this age [25]. Blocking I_{Nap} prevented plateau potential activity, PP-V1^R becoming unexcitable, and turned repetitive spiking V1^R into single spiking V1^R [25]. Therefore, we hypothesized that the different firing patterns of V1^R observed at E12.5 were related to the G_{Nap} / G_{Kdr} ratio only, with variations in the intensity of I_A being unlikely to account for the heterogeneity of firing pattern. We found that this ratio was significantly lower for SS V1^R recorded at E12.5 (G_{Nap} / G_{Kdr} = 0.043 ± 0.015, n = 9) compared to RS V1^R (0.154 ± 0.022, n = 8) and PP V1^R (0.66 ± 0.132, n = 6) (***Figure 1F***). We also found that the G_{Nap} / G_{Kdr} ratio was significantly lower for RS V1^R compared to PP V1^R (***Figure 1F***).

Altogether, these results strongly suggest that, although the presence of I_{Nap} is required for embryonic V1^R to fire repetitively or to generate plateau potentials [25], the heterogeneity of the firing pattern observed between E12.5 is not determined by I_{Nap} *per se* but likely by the balance between I_{Nap} and I_{Kdr}.

Manipulating the balance between G_{Nap} and G_{Kdr} changes embryonic V1^R firing patterns

We previously showed that blocking I_{Nap} with riluzole converted PP V1^R or RS V1^R into SS V1^R [25]. To confirm further that the balance between G_{Nap} and G_{Kdr} was the key factor in the heterogeneity of V1^R firing patterns, we assessed to what extent a given E12.5 SS V1^R cell could change its firing pattern when I_{Kdr} was gradually blocked by 4-aminopiridine (4-AP). We found that I_{Kdr} could be blocked by micromolar concentrations of 4-AP without affecting I_A (***Figure 2—figure supplement 1***). 4-AP, applied at concentrations ranging from 0.3 μM to 300 μM, specifically inhibited I_{Kdr} with an IC_{50} of 2.9 μM (***Figure 2—figure supplement 1C1***).

We then determined to what extent increasing the concentration of 4-AP modified the firing pattern of V1^R at E12.5. Applying 4-AP at concentrations ranging from 3 μM to 300 μM changed the firing pattern of SS V1^R (n = 10; N = 10) in a concentration-dependent manner (***Figure 2A1–A3***). In 50% of the recorded V1^R, increasing 4-AP concentrations successfully transformed SS V1^R into PP V1^R with the following sequence: SS → RS → ME → PP (***Figure 2A1***). In a second group of embryonic V1^R (25%), 4-AP application only evoked mixed activity, with the same sequence as aforementioned (SS → RS → ME) (data not shown). In the remaining SS V1^R (25%), increasing 4-AP concentration only led to sustained AP firing (***Figure 2A2***). Application of 300 μM 4-AP on RS V1^R at E12.5 evoked mixed events or plateau potentials (***Figure 2—figure supplement 2***). Plateau potentials and

169 repetitive spiking evoked in the presence of 300 μM 4-AP were fully blocked by 0.5-1 μM
170 TTX, indicating that they were generated by voltage-gated Na^+ channels (***Figure 2B,C*** and
171 ***Figure 2—figure supplement 2***). It should be noted that the application of 300 μM of 4-AP
172 induced a significant 30.5 ± 12.4 % increase (*P* = 0.0137; Wilcoxon test) of the input
173 resistance (1.11 ± 0.08 GΩ versus 1.41 ± 0.12 GΩ; n = 11; N = 11).
174 These results show that, in addition to I_{Nap}, I_{Kdr} is also a major determinant of the
175 firing pattern of embryonic $V1^R$. The above suggests that the firing patterns depend on a
176 synergy between I_{Nap} and I_{Kdr} and that the different patterns can be ordered along the
177 following sequence SS → RS → ME → PP when the ratio $G_{Nap}/\ G_{Kdr}$ is increased.
178
179 **The heterogeneity of the $V1^R$ firing patterns decreases during embryonic development**
180 It was initially unclear whether these different firing patterns corresponded to well
181 separated classes within the E12.5 $V1^R$ population or not. To address this question, we
182 performed a hierarchical cluster analysis on 163 embryonic $V1^R$, based on three
183 quantitative parameters describing the firing pattern elicited by the depolarizing pulse: the
184 mean duration of evoked APs or plateau potentials measured at half-amplitude (mean
185 ½Ad), the variability of the event duration during repetitive firing (coefficient of variation of
186 ½Ad: CV ½Ad) and the total duration of all events, expressed in percentage of the pulse
187 duration (depolarizing duration ratio: ddr) (***Figure 3A inserts***). In view of the large
188 dispersion of mean ½Ad and ddr values, cluster analysis was performed using the (decimal)
189 logarithm of these two quantities [40]. The analysis of the distribution of log mean ½Ad, CV
190 ½Ad and log ddr revealed multimodal histograms that could be fitted with several
191 Gaussians (***Figure 3—figure supplement 1A1–C1*****)**. Cluster analysis based on these three
192 parameters showed that the most likely number of clusters was 5 (***Figure 3A,B***), as

193 determined by the silhouette width measurement (***Figure 3B***). Two clearly separated
194 embryonic $V1^R$ groups with CV ½Ad = 0 stood out, as shown in the 3D plot in ***Figure 5C***. The
195 cluster with the largest ½Ad (mean ½Ad = 833.5 ± 89.99 ms) and the largest ddr (0.441 ±
196 0.044) contained all PP $V1^R$ (n = 35; N = 29) (***Figure 3C-D*** and ***Figure 3—figure supplement***
197 ***1A2,C2***). Similarly, the cluster with the shortest ½Ad (9.73 ± 0.66 ms) and the lowest ddr
198 (0.0051 ± 0.0004) contained all SS $V1^R$ (n = 46; N = 37) (***Figure 3C-D*** and ***Figure 3—figure***
199 ***supplement 1A2,C2***).

200 The three other clusters corresponded to $V1^R$ with nonzero values of CV ½Ad (***Figure 3C***).
201 A first cluster regrouping all RS $V1^R$ (n = 69; N = 61) was characterized by smaller values of
202 ½Ad (23.91 ± 1.43 ms), CV ½Ad (27.36 ± 1.64%) and ddr (0.11 ± 0.01) (***Figure 3C-D*** and
203 ***Figure 3—figure supplement 1A2,C2***). The last two clusters corresponded to ME $V1^R$
204 (***Figure 3C,D***). The smaller cluster, characterized by a larger CV ½Ad (170.9 ± 8.9%; n= 4; N =
205 4), displayed a mix of APs and short plateau potentials, while the second cluster, with
206 smaller CV ½Ad (87.61 ± 7.37%; n = 9; N = 9), displayed a mix of APs and long-lasting
207 plateau potentials (***Figure 3D*** and ***Figure 3—figure supplement 1B2***). Their ½Ad and ddr
208 values were not significantly different (***Figure 3—figure supplement 1A2,C2***).

209 It must be noted that three embryonic $V1^R$ (1.8%) were apparently misclassified since
210 they were aggregated within the RS cluster although having zero CV ½Ad (***Figure 3C;***
211 ***arrows***). Examination of their firing pattern revealed that this was because they generated
212 only two APs, although their ddr (0.16 to 0.2) and ½ Ad values (31.6 to 40.3 ms) were well
213 in the range corresponding of the RS cluster.

214 These different firing patterns of $V1^R$ might reflect different states of neuronal
215 development [31, 41-43]. Single spiking and/or plateau potentials are generally believed to
216 be the most immature forms of firing pattern, repetitive spiking constituting the most

mature form [19, 44]. If it were so, the firing patterns of embryonic $V1^R$ would evolve during embryonic development from single spiking or plateau potential to repetitive spiking, this latter firing pattern becoming the only one in neonates [26] and at early postnatal stages [27]. However, RS neurons already represent 41% of $V1^R$ at E12.5. We therefore analyzed the development of firing patterns from E11.5, when $V1^R$ terminate their migration and reach their final position [45], to E16.5. This developmental period covers a first phase of development (E11.5-E14.5), where lumbar spinal networks exhibit SNA, and a second phase (E14.5-E16.5), where locomotor-like activity emerges [4, 11, 46, 47]. We first analyzed changes in the intrinsic properties (input capacitance C_{in}, input resistance $R_{in} = 1/G_{in}$ and spike voltage threshold) of $V1^R$. C_{in} did not change significantly from E11.5 to E13.5 (***Figure 4A1***), remaining of the order of 12 pF, in agreement with our previous work [25]. However, it increased significantly at the transition between the two developmental periods (E13.5-E15.5) to reach about 23.5 pF at E15.5 (***Figure 4A1***). A similar developmental pattern was observed for R_{in}, which remained stable during the first phase from E11.5 to E14.5 ($R_{in} \approx$ 1-1.2 GΩ) but decreased significantly after E14.5 to reach about 0.7 GΩ at E15.5 (***Figure 4A2***). Spike threshold also decreased significantly between the first and the second developmental phases, dropping from about -34 mV at E12.5 to about -41 mV at E16.5 (***Figure 4A3***). Interestingly, this developmental transition around E14.5 correspond to the critical stage at which SNA gives way to a locomotor-like activity [11, 46, 47] and rhythmic activity becomes dominated by glutamate release rather than acetylcholine release [4].

This led us to hypothesize that this developmental transition could be also critical for the maturation of $V1^R$ firing patterns. The distinct firing patterns observed at E12.5 were already present at E11.5 (***Figure 4B1,C***), but the percentage of RS $V1^R$ strongly increased

241 from E11.5 to E12.5, while the percentage of ME V1^R decreased significantly (***Figure 4C***).
242 The heterogeneity of V1^R firing patterns then substantially diminished. Plateau potentials
243 were no longer observed at E13.5 (***Figure 4B2,C***), and ME V1^R disappeared at E14.5 (***Figure***
244 ***4B3,C***). Interestingly, the proportion of SS V1^R remained high from E13.5 to E15.5 and even
245 slightly increased (91.23% at E14.5 and 93.33% at E15.5; ***Figure 4C***). This trend was partially
246 reversed at E16.5, as the percentage of RS V1^R increased at the expense of SS V1^R (67.86%
247 SS V1^R and 32.34% RS V1^R; ***Figure 4B5,C***). This decrease in repetitive firing capability after
248 E13.5 was surprising in view of what is classically admitted on the developmental pattern
249 of neuronal excitability [18, 48]. Therefore, we verified that it did not reflect the death of
250 some V1^R after E13.5. Our data did not reveal any activated caspase3 (aCaspase3) staining
251 in V1^R (FoxD3 staining) at E14.5 (n = 10 SCs; N = 10) (***Figure 5***), in agreement with previous
252 reports showing that developmental cell death of V1^R does not occur before birth [49].

253 To determine whether G_{Nap} and G_{Kdr} also controlled the firing pattern of V1^R at E14.5
254 (see ***Figure 4B3,C***), we assessed the presence of I_{Nap} and I_{Kdr} in single spiking V1^R at this
255 embryonic age. Both I_{Nap} and I_{Kdr} were present in V1^R at E14.5 (***Figure 6—figure***
256 ***supplement 1*** **and** ***Figure 6—figure supplement 2*****)** whereas, as in V1^R at E12.5, no calcium-
257 dependent potassium current was detected at this developmental age (not shown). In SS
258 V1^R, G_{Kdr} was significantly higher at E14.5 (11.11 ± 1.12 nS, n = 10; N = 10) than at E12.5
259 (***Figure 1D***). In contrast, G_{Nap} was similar at E14.5 (0.13 ± 0.14 nS, n = 10; N = 10) and E12.5
260 **(*Figure 1E***). We also found that the G_{Nap} / G_{Kdr} ratio was significantly lower for SS V1^R
261 recorded at E14.5 (0.012 ± 0.004, n = 10) compared to RS V1^R (0.154 ± 0.022, n = 8) and PP
262 V1^R (0.66 ± 0.132, n = 6) recorded at E12.5 (***Figure 1F***).

263 We tested the effect of 4-AP in SS V1^R at E14.5. At this embryonic age, 300 μM 4-AP
264 inhibited only 59.2% of I_{Kdr}. Increasing 4-AP concentration to 600 μM did not inhibit I_{Kdr}

significantly more (60.2%) (***Figure 6—figure supplement 2***), indicating that inhibition of I_{Kdr} by 4-AP reached a plateau at around 300 μM. 600 μM 4-AP application had no significant effect on I_A (***Figure 6—figure supplement 2***). The application of the maximal concentration of 4-AP tested (600 μM) converted SS $V1^R$ (n = 13; N = 13) to PP $V1^R$ (23.1%; ***Figure 6A1,B***), RS $V1^R$ (38.5%; ***Figure 6A2,B***) or ME $V1^R$ (38.4%; ***Figure 6B***), as was observed at E12.5, thus indicating that the firing pattern of $V1^R$ depends on the balance between I_{Nap} and I_{Kdr} also at E14.5. Plateau potential and repetitive spiking recorded in the presence of 4-AP at E14.5 were fully blocked by 0.5-1 μM TTX indicating that they were generated by voltage-gated sodium channels (***Figure 6A1,A2***), as observed at E12.5.

Theoretical analysis: the basic model

As shown in ***Figure 7A*** for 26 cells, in which both G_{Nap} and G_{Kdr} were measured, the three largest clusters revealed by the hierarchical clustering analysis (SS, RS and PP, which account together for the discharge of more than 95% of cells, see ***Figure 5***) correspond to well defined regions of the G_{Nap}- G_{Kdr} plane. Single spiking is observed only when G_{Nap} is smaller than 0.6 nS. For larger values of G_{Nap}, repetitive spiking occurs when G_{Kdr} is larger than 3.5 nS, and $V1^R$ display plateau potentials when G_{Kdr} is smaller than 3.5 nS. Mixed events (ME, 4.5% of the 163 cells used in the cluster analysis), where plateaus and spiking episodes alternate, are observed at the boundary of RS and PP clusters. This suggested to us that a conductance-based model incorporating only the leak current, I_{Nat}, I_{Nap} and I_{Kdr} (see Materials and Methods) could account for most experimental observations, the observed zonation being explained in terms of bifurcations between the different stable states of the model. Therefore, we first investigated a simplified version of the model without I_A and slow inactivation of I_{Nap}.

A one-parameter bifurcation diagram of this "basic" model is shown in ***Figure 7B*** for two values of G_{Kdr} (2.5 nS and 10 nS) and a constant injected current I = 20 pA. In both cases, the steady-state membrane voltage (stable or unstable) and the peak and trough voltages of stable and unstable periodic solutions are shown as the function of the maximal conductance G_{Nap} of the I_{Nap} current, all other parameters being kept constant. For G_{Kdr} = 10 nS, the steady-state membrane voltage progressively increases (in gray) with G_{Nap}, but repetitive spiking (in red, see voltage trace for G_{Nap} = 1.5 nS) is not achieved until G_{Nap} reaches point SN_1, where a saddle node (SN) bifurcation of limit cycles occurs. This fits with the experimental data, where a minimal value of G_{Nap} is required for repetitive spiking (see also [25]), and is in agreement with the known role of I_{Nap} in promoting repetitive discharge [50, 51]. Below SN_1, the model responds to the onset of a current pulse by firing only one spike before returning to quiescence (see voltage trace for G_{Nap}= 0.2 nS), or a few spikes when close to SN_1 (not shown) before returning to quiescence. The quiescent state becomes unstable through a subcritical Hopf bifurcation (HB) at point HB_1, with bistability between quiescence and spiking occurring between SN_1 and HB_1 points. Repetitive firing persists when G_{Nap} is increased further and eventually disappears at point SN_2. The firing rate does not increase much throughout the RS range (***Figure 7—figure supplement 1C***), remaining between 20.1 Hz (at SN_1) and 28.7 Hz (at SN_2). A stable plateau appears at point HB_2 through a subcritical HB. The model is bistable between HB_2 and SN_2, with plateau and large amplitude APs coexisting in this range.

The model behaves very differently when G_{Kdr} is reduced to 2.5 nS (gray-blue curve in ***Figure 7B***). It exhibits a unique stable fixed point whatever the value of G_{Nap} is, and the transition from quiescence to plateau is gradual as G_{Nap} is increased. No repetitive spiking is ever observed. This indicates that the activity pattern is controlled not only by G_{Nap} but

313 also by G_{Kdr}. This is demonstrated further in ***Figure 7C***, where G_{Nap} was fixed at 1.2 nS
314 while G_{Kdr} was increased from 0 to 25 nS. The model exhibits a plateau potential until
315 G_{Kdr} is increased past point the subcritical HB point HB_2, repetitive spiking sets in before at
316 point SN_2 *via* a SN of limit cycles bifurcation. When G_{Kdr} is further increased, repetitive
317 firing eventually disappears through a SN bifurcation of limit cycles at point SN_1, the
318 quiescent state becomes stable through a subcritical HB at point HB_1, and bistability occurs
319 between these two points. This behavior is in agreement with ***Figure 7A***.
320 Since both conductances G_{Nap} and G_{Kdr} control the firing pattern of embryonic $V1^R$ cells,
321 we computed a two-parameters bifurcation diagram (***Figure 7D***), where the stability
322 regions of the different possible activity states and the transition lines between them are
323 plotted in the G_{Nap} - G_{Kdr} plane. The black curves correspond to the bifurcations HB_1 and
324 HB_2 and delimit a region where only repetitive firing occurs. The red curves correspond to
325 the SN bifurcations of periodic orbits associated with the transition from quiescence to
326 firing (SN_1) and the transition from plateau to firing (SN_2). They encompass a region
327 (shaded area) where repetitive firing can be achieved but may coexist with quiescence
328 (between the HB_1 and SN_1 lines) or plateau potential (in the narrow region between the
329 HB_2 and SN_2 lines).
330 Some important features of the diagram must be emphasized: 1) minimal values of both
331 G_{Nap} (to ensure sufficient excitability) and G_{Kdr} (to ensure proper spike repolarization) are
332 required for repetitive spiking, 2) quiescence and plateau can be clearly distinguished only
333 when they are separated by a region of repetitive spiking (see also ***Figure 7B*** for G_{Kdr} = 10
334 nS), otherwise the transition is gradual (***Figure 7B*** for G_{Kdr}= 2.5 nS), 3) only oblique lines
335 with an intermediate slope cross the bifurcation curve and enter the RS region (see, for
336 example, the red line in ***Figure 7D***). This means that repetitive spiking requires an

appropriate balance between I_{Nap} and I_{Kdr}. If the ratio G_{Nap}/G_{Kdr} is too large (blue line) or too small (gray line), only plateau potentials or quiescence will be observed at steady state. This is exactly what is observed in experiments, as shown by the cumulative distribution function of the ratio G_{Nap}/G_{Kdr} for the different clusters of embryonic $V1^R$ in ***Figure 7E*** (same cells as in ***Figure 7A***). The ratio increases according to the sequence SS → RS → ME → PP, with an overlap of the distributions for SS $V1^R$ and RS $V1^R$. Note also that the ratio for ME cells (around 0.25) corresponds to the transition between repetitive spiking and plateau potentials (more on this below).

Embryonic $V1^R$ cells display voltage fluctuations that may exceed 5 mV and are presumably due to channel noise. The relatively low number of sodium and potassium channels (of the order of a few thousands) led to voltage fluctuations in the stochastic version of our model comparable to those seen experimentally when the cell was quiescent (top voltage trace in ***Figure 7D***) or when a voltage plateau occurred (bottom trace). Channel noise caused some jitter during repetitive spiking (middle trace), and induced clearly visible variations in the amplitude of APs. However, repetitive firing proved to be very robust and was not disrupted by voltage fluctuations. Altogether, channel noise little alters the dynamics (compare the deterministic voltage traces in ***Figure 7B*** and the noisy traces in ***Figure 7D***). This is likely because channel noise has a broad power spectrum and displays no resonance with the deterministic solutions of the model.

The one-parameter bifurcation diagram of the model was not substantially modified when we took I_A into account, as shown in ***Figure 6—figure supplement 1***. It just elicited a slight membrane hyperpolarization, an increase in the minimal value of G_{Nap} required for firing, and a decrease of the firing frequency. The transition from repetitive firing to plateau was not affected because I_A is then inactivated by depolarization.

The bifurcation diagram of ***Figure 7D*** accounts *qualitatively* for the physiological data on $V1^R$ at E12.5 presented in ***Figure 7A***, as shown in ***Figure 7F*** where the conductance data of ***Figure 7A*** were superimposed on it. However, one must beware of making a more *quantitative* comparison because the theoretical bifurcation diagram was established for a constant injected current of 20 pA, whereas the current injected in experiments data varied from neuron to neuron and ranged from 10 to 30 pA in the sample shown in ***Figure 7A***. The position of bifurcation lines in the G_{Nap} - G_{Kdr} plane depends not only on the value of the injected current, but on the values chosen for the other parameters, which also vary from cell to cell but were kept at fixed values in the model [52]. For instance, the diagrams were computed in ***Figure 7D,F*** for G_{in}= 1 nS and C_{in}= 13 pF, the median values of the input conductance and capacitance at E12.5, taking no account of the cell-to-cell variations of these quantities. Between E12.5 and E14.5, C_{in} which provides an estimate of the cell size, increases by 38% in average, whereas G_{in} is not significantly modified (see ***Figure 4***). As illustrated in ***Figure 7G*** the two-parameters bifurcation diagram is then shifted upward and rightward compared to ***Figure 7F***, because larger conductances are required to obtain the same firing pattern. The observed regression of excitability from E12.5 to E14.5-E15.5 (see ***Figure 4C***) thus comes from a decrease in G_{Nap} density (see presumable developmental trajectories indicated by arrows in ***Figure 7F***) together with a shift of the RS region as cell size increases. As a result, all 10 cells shown in ***Figure 7G*** are deeply inside the SS region at E14.5.

It is less straightforward to explain on the basis of our model the experiments where 4-AP changed the firing pattern of SS $V1^R$ (***Figure 2***). Indeed, the decrease of G_{Kdr} (***Figure 6—figure supplement 2***), although it may exceed 70% at the higher concentrations of 4-AP we used, is not sufficient by itself to account for the change in the firing pattern of $V1^R$ (***Figure***

385 ***6—figure supplement 2***) because data points in the SS cluster will not cross the bifurcation
386 lines between SS and RS (SN1) and between RS and PP (SN2) when displaced downward in
387 the G_{Nap}- G_{Kdr} plane. However, 4-AP at a 300 μM concentration also decreases G_{in} (by 23%
388 in average and up to 50% in some neurons), the rheobase current with it, and the current
389 that was injected in cells during experiments was reduced accordingly. hen we take into
390 account this reduction of both G_{in} and I the two parameters bifurcation diagram pf the
391 model remains qualitatively the same, but it is shifted leftward and downward in the G_{Nap}-
392 G_{Kdr} plane (***Figure 6—figure supplement 2***). As a consequence, the bifurcation lines
393 between SS and RS and between RS and PP (SN2) are then successively crossed when
394 G_{Kdr} is reduced, in accordance with experimental results.
395
396 **Theoretical analysis: slow inactivation of $\mathbf{I_{Nap}}$ and bursting**
397 Our basic model accounts for the firing pattern of 73% of the 163 cells used in the
398 cluster analysis. However, bursting, under the form of recurring plateaus separated by brief
399 repolarization episodes (see a typical trace in ***Figure 8A left***), was experimentally observed
400 in half of PP $V1^R$ (24 out of 46), and plateaus intertwined with spiking episodes were
401 recorded in the 13 cells of the ME cluster (8% of the total sample, see ***Figure 8A right*** for a
402 typical example). Recurrent plateaus indicate membrane bistability and require that the
403 $I - V$ curve be S-shaped. This occurs when G_{Nap} is large and G_{Kdr} small. (***Figure 8B1,B2***).
404 However, our basic model lacks a mechanism for switching between quiescent state and
405 plateau, even in this case. Channel noise might induce such transitions, but our numerical
406 simulations showed that this is too infrequent to account for bursting (see voltage trace in
407 ***Figure 8B1*** where the plateau state is maintained despite channel noise).

To explain recurrent plateaus during a constant current pulse, we have to incorporate in our model an additional slow dynamical process. Therefore, we took into account the slow inactivation of I_{Nap} that is observed in experiments. I_{Kdr} also inactivates slowly but over times that are much longer than the timescale of bursting, which is why we did not take its slow inactivation into account. The one-parameter bifurcation diagram of the basic model without slow inactivation of I_{Nap} is shown in ***Figure 8C*** for G_{Kdr} = 5 nS and an injected current reduced to 10 pA (as compared to 20 pA in the previous section), so as to allow for bistability (see ***Figure 8B2***). The $G_{Nap} - V$ curve is then S-shaped, as shown in ***Figure 8B1***, with a bistability region for G_{Nap} between 1.36 and 1.85 nS. This is in contrast with ***Figure 7B*** where the $G_{Nap} - V$ curve was monotonic. Adding the slow (de)inactivation of I_{Nap} then causes periodic transitions between up (plateau) and down (quiescent) states, as illustrated by the top voltage trace on the right of ***Figure 8C***, and the model displayed a stable limit cycle (shown in black in the bifurcation diagram on the left of ***Figure 8C***). This mechanism is known as pseudo-plateau or plateau-like bursting (a.k.a. fold-subcritical HB bursting) [53]. In contrast with square wave bursting [54-57], where the up-state is a stable limit cycle arising from a supercritical Hopf bifurcation [58-60], the up-state here is a stable fixed point (which coexists with an unstable limit cycle). This is why one does not observe bursts of APs separated by quiescent periods as, for instance, observed in postnatal CA1 Pyramidal cells [61] and in neurons of neonatal pre-Bötzinger Complex [62, 63], but recurrent plateaus. The duration of the plateaus and repolarization episodes depends on the values of G_{Nap} and G_{Kdr}. A voltage-independent time constant $\tau_s = 2\ ms$ leads to up and down states of comparable durations (see top left voltage trace in ***Figure 8C***). In agreement with the bifurcation diagram of ***Figure 8C***, the persistent sodium current inactivates during plateaus (phase 1, see bottom right trace in in ***Figure 8C***) and de-

inactivates during quiescent episodes (phase 3, see bottom right trace). Transitions from the down-state to the up-state occurs when inactivation has reached its maximal value (phase 2) and transition from the up-state to the down state when it has reached its maximum (phase 4). Adding channel noise preserves bursting but introduces substantial randomness in the duration of plateaus and repolarization episodes (bottom left voltage trace in ***Figure 8C***). Moreover, it substantially decreases the duration of both plateaus and quiescent episodes by making transition between the two states easier (compare the top and bottom voltage traces on the left, both computed for $\tau_s = 2\ ms$).

Increasing G_{Nap} (or decreasing G_{Kdr}) makes plateaus much longer than quiescent episodes (see bottom right voltage trace in ***Figure 8C***). This again points out to the fact that the ratio is an important control parameter. We also noted that adding the I_A current lengthened the quiescence episodes (***Figure 6–figure supplement 1***).

Slow inactivation of I_{Nap} also provides an explanation for mixed patterns, where plateaus alternate with spiking episodes (***Figure 8A, right***). They take place in our model near the transition between repetitive spiking and plateau, as in experiments (see ***Figure 8A***). Slow inactivation can lead to elliptic bursting, notably when the bifurcation HB_2 is subcritical [64, 65], which is the case here (***Figure 8D***). The model then displays a stable limit cycle with alternating plateaus and spiking episodes, arising from crossing the bifurcation points HB_2 and SN_2 back and forth (see bifurcation diagram in ***Figure 8D*** and top voltage trace). We note that sufficient de-inactivation of I_{Nap} for triggering a new plateau (phase 3 in the bottom trace of ***Figure 8D***) may be difficult to achieve during spiking episodes, because voltage oscillates over a large range, which tends to average out the variations of the inactivation level. If de-inactivation is not sufficient, the model keeps on spiking repetitively without returning to the plateau state. This is what occurs for cells

well within the RS region, far away from the RS-PP transition. It also probably explains why it was difficult in many recorded cells to elicit plateaus by increasing the injected current, inactivation balancing then the increase of I_{Nap} induced by the larger current.

Altogether, our study shows that a model incorporating the slow inactivation of I_{Nap} accounts for all the firing patterns displayed by cells from the PP and ME clusters.

Discussion

$V1^R$ constitute a homogeneous population when referring to their transcription factor program during development [24, 66], their physiological function [67] and their firing pattern at postnatal stages [27]. Surprisingly, our electrophysiological recordings and our cluster analysis clearly indicate that distinct functional classes of $V1^R$ are transiently present during development at the onset of the SNA (E11.5-E12.5). Five different groups of embryonic $V1^R$ were defined using cluster analysis, according to their firing properties.

Development of the firing pattern of embryonic $V1^R$ during SNA

It is generally assumed that, during early development, newborn neurons cannot sustain repetitive firing [35, 48]. Later on, neurons progressively acquire the ability to fire repetitively, APs become sharper, and neurons eventually reach their mature firing pattern, due to the progressive appearance of a panoply of voltage-gated channels with different kinetics [18, 35, 48]. Our results challenge the general view that single spiking is a more primitive form of excitability [35]. Indeed, we show that repetitive firing and plateau potentials dominated at early stages (E11.5-E12.5), while single spiking was prevailing only later (E13.5- E16.5).

The different $V1^R$ firing patterns observed at E11.5-E12.5 might reflect variability in the maturation level between $V1^R$ at a given developmental stage, as suggested for developing MNs [68, 69]. However, this is unlikely since $V1^R$ transiently lose their ability to sustain tonic firing or plateau potential after E13.5. The heterogeneous discharge patterns of $V1^R$ observed before E13.5 contrasts with the unique firing pattern of $V1^R$ at postnatal age [27]. Accordingly, the transient functional heterogeneity of $V1^R$ rather reflects an early initial developmental stage (E11.5-E13.5) of intrinsic excitability.

The physiological meaning of the transient functional involution of $V1^R$ that follows, after E12.5, is puzzling. To our knowledge, such a phenomenon was never described in vertebrates during CNS development. So far, a functional involution was described only for inner hair cells between E16 and P12 [70, 71] and cultured oligodendrocytes [72], and it was irreversible. Because most $V1^R$ cannot sustain tonic firing after E12.5, it is likely that their participation to SNA is limited to the developmental period before other GABAergic interneuron subtypes mature and start to produce GABA and glycine [73]. Interestingly, embryonic $V1^R$ begin to recover their capability to sustain tonic firing when locomotor-like activity emerges [4, 11], a few days before they form their recurrent synaptic loop with MNs (around E18.5 in the mouse embryos, [74]). One possible function of the transient involution between E12.5 and E15.5 could be to regulate the growth of $V1^R$ axons toward their targets. It is indeed known that low calcium fluctuations within growth cones are required for axon growth while high calcium fluctuations stop axon growth and promote growth cone differentiation [75].

Ion channels mechanisms underlying the functional heterogeneity of embryonic $V1^R$

Blockade of I_{Nap} leads to single spiking [25], which emphasizes the importance of this current for the occurrence of repetitive firing and plateau potentials in $V1^R$ at early developmental stages. But these neurons can also switch from one firing pattern to another, when G_{Kdr} is decreased by 4-AP, which emphasizes the importance of I_{Kdr}. We found that the main determinant of embryonic $V1^R$ firing pattern is the balance between G_{Nap} and G_{Kdr}.

A Hodgkin-Huxley-type model incorporating a persistent sodium current I_{Nap} provided a parsimonious explanation of all five firing patterns recorded in the $V1^R$ population at E12.5. It provided a mathematical interpretation for the clustering of embryonic $V1^R$ shown by the hierarchical analysis and accounted for the effect of 4-AP and riluzole [25] on the discharge. Remarkably, it highlighted how a simple mechanism involving only the two opposing currents I_{Nap} and I_{Kdr}, but not I_A, could produce functional diversity in a population of developing neurons. The model explained why minimal G_{Nap} and G_{Kdr} are required for firing, and how a synergy between G_{Nap} and G_{Kdr} controls the firing pattern and accounts for the zonation of the $G_{Nap} - G_{Kdr}$ plane that is observed experimentally.

Taking into account the slow inactivation of I_{Nap} to the model allowed us to explain the bursting patterns displayed by cells of the PP and ME clusters. We showed, in particular, that mixed events arose from elliptic bursting at the repetitive spiking-plateau transition and that smooth repetitive plateaus could be explained by a pseudo-plateau bursting mechanism [53, 59]. Such bursting scenario has been previously studied in models of endocrine cells [58, 76, 77] and adult neurons [78], but rarely observed in experiments [79]. It contrasts with the more common square wave bursting at firing onset, i.e. alternating bursts of APs and quiescent episodes, on which most studies of bursting focused [61-63]. Our model can also display such square wave bursting, but this occurs for physiologically

526 realistic parameter values, and did not dwell on that bursting mode that we never
527 observed in embryonic V1^R. The model also provides a mathematical explanation for mixed
528 events, where bursts of APs alternate with plateau episodes. It is due to an elliptic bursting
529 scenario at the RS-PP transition, a firing range that the afore-mentioned studies did not
530 examine. This further emphasizes the capacity of our simple model to account for a wide
531 diversity of firing patterns.

532 Pseudo-plateau bursting has also been observed in the embryonic pre-Bötzinger
533 network [79]. However, it is produced there by the calcium-activated nonselective cationic
534 current I_{CAN}, while I_{Nap} leads to square wave bursting. Pseudo-plateau bursting, displayed
535 by half of the cells at E16.5 largely disappears at E18.5 because of the change in the
536 balance between I_{CAN} and I_{Nap} during embryonic maturation [79]. Such a scenario cannot
537 account for the variety of discharge patterns observed in embryonic V1^R at the E11.5-12.5
538 stage of development. Our theoretical analysis and our experimental data clearly indicate
539 that the interplay between two opposing currents is necessary to explain all the firing
540 patterns of V1^R. Our model is of course not restricted to embryonic V1^R, but may also apply
541 to any electrically compact cell, the firing activity of which is dominated by I_{Nap} and
542 delayed rectifier potassium currents. This is the case of many classes of embryonic cells in
543 mammals at an early stage of their development. It can also apply to the axon initial
544 segment, where G_{Nap} and G_{Kdr} are known to play the major role in the occurrence of
545 repetitive firing [80].

546 Altogether our experimental and theoretical results provide a global view of the
547 developmental trajectories of embryonic V1^R (see ***Figure 7F, G***). At E12.5, conductances of
548 embryonic V1^R are widely spread in the $G_{Nap} - G_{Kdr}$ plane, which explains the
549 heterogeneity of their firing patterns. This likely results from the random and uncorrelated

550 expression of sodium and potassium channels from cell to cell at this early stage. Between
551 E12.5 and E14.5-15.5 cell size increases, and G_{Kdr} with it, while the density of sodium
552 channels decreases (see ***Figures 1 and 4***). The functional involution displayed by $V1^R$
553 between E12.5 and E15.5 thus mainly results from a decrease of G_{Nap} coordinated with an
554 increase of G_{Kdr}. How these synergistic processes are controlled during this developmental
555 period remains an open issue.

556 It is important to note that the presence of I_{Nap} is required for the functional diversity
557 of $V1^R$. Indeed, in the absence of I_{Nap}, $V1^R$ lose their ability to generate plateau potentials
558 or to fire repetitively. More generally, when the diversity of voltage-gated channels is
559 limited, as observed in embryonic neurons [18], changes in the balance between I_{Kdr} and
560 non (or poorly) inactivating inward current can modify the firing pattern. This can be
561 achieved not only by I_{Nap}, but also by other slowly or non-inactivating inward
562 conductances, such as I_{CAN} [79]. Our work also clearly indicates that a change in the firing
563 pattern can only occur if a change in inward conductances cannot be counterbalanced by a
564 corresponding change in outward conductances. This implies that there is no homeostatic
565 regulation of channel density to ensure the robustness of $V1^R$ excitability during its early
566 development, contrarily to the mature CNS [37]. In addition, the poor repertoire of
567 voltage-gated channels at this developmental stage precludes channel degeneracy, which
568 is also known to ensure the robustness of excitability in mature neurons [37].

569 In conclusion, our study shows that there is no universal pattern of development in
570 embryonic neurons, and it demonstrates that a simple general mechanism involving only
571 two slowly inactivating voltage-gated channels with opposite effects is sufficient to
572 produce

573 a wide variety of firing patterns in immature neurons having a limited repertoire of
574 voltage-gated channels.
575

576

577 # Materials and Methods

Key Resources Table				
Reagent type (species) or resource	**Designation**	**Source or reference**	**Identifiers**	**Additional information**
genetic reagent (M. musculus Swiss) male and female	GAD1^{GFP}	PMID: 14574680		a cDNA encoding enhanced GFP (eGFP) was targeted to the locus encoding the gene Gad1.
Antibody	Anti-FoxD3 (Guinea pig polyclonal)	PMID:19088088		IF(1:5000)
Antibody	Anti-cleaved Caspase-3 (Asp175) (Rabbit polyclonal)	Cell Signaling Technology	Cat# 9661, RRID: AB_2341188	IF(1:1000)
chemical compound, drug	Tetrodotoxin	Alomone labs	Cat# T550, CAS No.: 18660-81-6	1 µM
chemical compound, drug	4-aminopyridine	Sigma-Aldrich	Cat# A78403, CAS No.: 504-24-5	0.3 - 600 µM
software, algorithm	pCLAMP 10.5	Molecular devices	RRID:SCR_014284	
software, algorithm	Axograph 1.7.2	AxoGraph	RRID:SCR_014284	
software, algorithm	PRISM 7.0e	GraphPad Software	RRID:SCR_002798)	
software, algorithm	ImageJ 1.5	N.I.H. (USA)	RRID:SCR_003070	

software, algorithm	Adobe Photoshop CS6	Adobe, USA	RRID:SCR_014199	
software, algorithm	R software 3.3.2	Cran project (https://cran.r-project.org/)	RRID:SCR_001905	
software, algorithm	XPP-Aut 8.0	University of Pittsburgh; Pennsylvania; USA	RRID:SCR_001996	

578

579 **Isolated spinal cord preparation**

580 Experiments were performed in accordance with European Community guiding principles
581 on the care and use of animals (86/609/CEE, CE Off J no. L358, 18 December 1986), French
582 decree no. 97/748 of October 19, 1987 (J Off République Française, 20 October 1987, pp.
583 12245-12248). All procedures were carried out in accordance with the local ethics
584 committee of local Universities and recommendations from the CNRS. We used Gad1^{GFP}
585 knock-in mice to visualize putative GABAergic INs [81], as in our previous study [25]. To
586 obtain E12.5-E16.5 Gad1^{GFP} embryos, 8 to 12 weeks old wild-type Swiss female mice were
587 crossed with Gad1^{GFP} Swiss male mice.
588 Isolated mouse SCs from 420 embryos were used in this work and obtained as previously
589 described [28, 82]. Briefly, pregnant mice were anesthetized by intramuscular injection of a
590 mix of ketamine and xylazine and sacrificed using a lethal dose of CO_2 after embryos of
591 either sex were removed. Whole SCs were isolated from eGFP-positive embryos and
592 maintained in an artificial cerebrospinal fluid (ACSF) containing 135 mM NaCl, 25 mM
593 $NaHCO_3$, 1 mM NaH_2PO_4, 3 mM KCl, 11 mM glucose, 2 mM $CaCl_2$, and 1 mM $MgCl_2$ (307
594 mOsm/kg H_2O), continuously bubbled with a 95% O_2-5% CO_2 gas mixture.

In the lumbar SC of Gad1^{GFP} mouse embryos, eGFP neurons were detected using 488 nm UV light. They were localized in the ventro-lateral marginal zone between the motor columns and the ventral funiculi [66]. Embryonic V1^{R} identity was confirmed by the expression of the forkhead transcription factor Foxd3 [25].

Whole-cell recordings and analysis

The isolated SC was placed in a recording chamber and was continuously perfused (2 ml/min) at room temperature (22-26°C) with oxygenated ACSF. Whole-cell patch-clamp recordings of lumbar spinal embryonic V1^{R} were carried out under direct visualization using an infrared-sensitive CCD video camera. Whole-cell patch-clamp electrodes with a resistance of 4-7 MΩ were pulled from thick-wall borosilicate glass using a P-97 horizontal puller (Sutter Instrument Co., USA). They were filled with a solution containing (in mM): 96.4 K methanesulfonate, 33.6 KCl, 4 $MgCl_2$, 4 Na_2ATP, 0.3 Na_3GTP, 10 EGTA, and 10 HEPES (pH 7.2; 290 mOsm/kg-H_2O). This intracellular solution led to an equilibrium potential of chloride ions, E_{Cl}, of about -30 mV, close to the physiological values measured at E12.5 in spinal MNs [28]. The junction potential (6.6 mV) was systematically corrected offline.

Signals were recorded using Multiclamp 700B amplifiers (Molecular Devices, USA). Data were low-pass filtered (2 kHz), digitized (20 kHz) online using Digidata 1440A or 1550B interfaces and acquired using pCLAMP 10.5 software (Molecular Devices, USA). Analyses were performed off-line using pCLAMP 10.5 software packages (Molecular devices; RRID:SCR_014284) and Axograph 1.7.2 (AxoGraph; RRID:SCR_002798).

In voltage-clamp mode, voltage-dependent K^+ currents (I_{Kv}) were elicited in the presence of 1 μM tetrodotoxin (TTX, Alomone lab, Cat# T550, CAS No.: 18660-81-6) by 500 ms depolarizing voltage steps (10 mV increments, 10 s interval) after a prepulse of 300 ms at

V_H = -100 mV. To isolate I_{Kdr}, voltage steps were applied after a 300 ms prepulse at V_H = -30 mV that inactivated the low threshold transient potassium current I_A. I_A was then obtained by subtracting offline I_{Kdr} from the total potassium current I_{Kv}. Capacitance and leak current were subtracted using on-line P/4 protocol provided by pCLAMP 10.5.

In current-clamp mode, $V1^R$ discharge was elicited using 2 s depolarizing current steps (from 0 to ≈ 50 pA in 5-10 pA increments, depending on the input resistance of the cell) with an 8 s interval to ensure that the membrane potential returned to V_H. When a cell generated a sustained discharge, the intensity of the depolarizing pulse was reduced to the minimal value compatible with repetitive firing.

I_{Nap} was measured in voltage-clamp mode using a 70 mV/s depolarizing voltage ramp [83]. This speed was slow enough to preclude substantial contamination by the inactivating transient current and fast enough to avoid substantial inactivation of I_{Nap}. Subtraction of the current evoked by the voltage ramp in the presence of 1 μM TTX from the control voltage ramp-evoked current revealed I_{Nap}.

Pharmacological reagents

During patch-clamp recordings, bath application of TTX (1 μM, Alomone lab, Cat# T550, CAS No.: 18660-81-6) or 4-aminopyridine (4-AP, Sigma Aldrich Cat# T550, CAS No.: 18660-81-6) was done using 0.5 mm diameter quartz tubing positioned, under direct visual control, 50 μm away from the recording area. The quartz tubing was connected to 6 solenoid valves linked with 6 reservoirs *via* a manifold. Solutions were gravity-fed into the quartz tubing. Their application was controlled using a VC-8 valve controller (Warner Instruments, USA).

4-AP was used to block I_{Kdr}. To determine the concentration–response curve, $I-V$ curves of I_{Kdr} for different concentrations of 4-AP (0.3 to 300 μM) were compared to the control curve obtained in the absence of 4-AP. The percentage of inhibition for a given concentration was calculated by dividing the peak intensity of I_{Kdr} by the peak value obtained in control condition. The obtained normalized concentration–response curves were fitted using the Hill equation:

$$\frac{100-I_{min}}{1+([4-AP]/IC_{50})^{n_H}}+I_{min}\ ,$$

where [4-AP] is the 4-AP concentration, I_{min} is the residual current (in percentage of the peak I_{Kdr}), $100-I_{min}$ is the maximal inhibition achieved for saturating concentration of 4-AP, IC_{50} is the 4-AP concentration producing half of the maximal inhibition, and n_H is the Hill coefficient. Curve fitting was performed using KaleidaGraph 4.5 (Synergy Software, USA).

Immunohistochemistry and confocal microscopy

E14.5 embryos were collected from pregnant females. Once dissected out of their yolk sac, SCs were dissected and immediately immersion-fixed in phosphate buffer (PB 0.1 M) containing 4% paraformaldehyde (PFA; freshly prepared in PB, pH 7.4) for 1 h at 4°C. Whole SCs were then rinsed out in 0.12 M PB at 4°C, thawed at room temperature, washed in PBS, incubated in NH_4Cl (50 mM), diluted in PBS for 20 min and then permeabilized for 30 min in a blocking solution (10% goat serum in PBS) with 0.2% Triton X-100. They were incubated for 48 h at 4°C in the presence of the following primary antibodies: guinea pig anti-FoxD3 (1:5000, gift from Carmen Birchmeier and Thomas Müller of the Max Delbrück Center for Molecular Medicine in Berlin) and rabbit anti-cleaved Caspase-3 (1:1000, Cell Signaling Technology Cat# 9661, RRID:AB_2341188). SCs were then washed in PBS and incubated for

2 h at RT with secondary fluorescent antibodies (goat anti-rabbit-conjugated 649; donkey anti-guinea pig-conjugated Alexa Fluor 405 [1:1000, ThermoFisher]) diluted in 0.2% Triton X-100 blocking solution. After washing in PBS, SCs were dried and mounted in Mowiol medium (Millipore, Molsheim, France). Preparations were then imaged using a Leica SP5 confocal microscope. Immunostaining was observed using a 40X oil-immersion objective with a numerical aperture of 1.25, as well as with a 63X oil-immersion objective with a numerical aperture of 1.32. Serial optical sections were obtained with a Z-step of 1 µm (40X) and 0.2-0.3 µm (63X). Images (1024x1024; 12-bit color scale) were stored using Leica software LAS-AF and analyzed using ImageJ 1.5 (N.I.H., USA, RRID:SCR_003070) and Adobe Photoshop CS6 (Adobe, USA, RRID:SCR_014199) software.

Cluster analysis

To classify the firing patterns of embryonic $V1^R$, we performed a hierarchical cluster analysis on a population of 163 cells. Each cell was characterized by three quantitative measures of its firing pattern (see legend of Figure 5). After normalizing these quantities to zero mean and unit variance, we performed a hierarchical cluster analysis using the hclust function in R 3.3.2 software (Cran project ; https://cran.r-project.org/; RRID:SCR_001905) that implements the complete linkage method. The intercluster distance was defined as the maximum Euclidean distance between the points of two clusters, and, at each step of the process, the two closest clusters were merged into a single one, thus constructing progressively a dendrogram. Clusters were then displayed in data space using the dendromat function in the R package 'squash' dedicated to color-based visualization of multivariate data. The best clustering was determined using the silhouette measure of clustering consistency [84]. The silhouette of a data point, based on the comparison of its

distance to other points in the same cluster and to points in the closest cluster, ranges from -1 to 1. A value near 1 indicates that the point is well assigned to its cluster, a value near 0 indicates that it is close to the decision boundary between two neighboring clusters, and negative values may indicate incorrect assignment to the cluster. This allowed us to identify an optimal number k of clusters by maximizing the overall average silhouette over a range of possible values for k [84], using the silhouette function in the R package 'cluster'.

Biophysical modeling

To understand the relationship between the voltage-dependent membrane conductances and the firing patterns of embryonic $V1^R$, we relied on a single compartment conductance-based model that included the leak current, the transient and persistent components of the sodium current, I_{Nat} and I_{Nap}, a delayed rectifier potassium current I_{Kdr} and the inactivating potassium current I_A revealed by experiments. Voltage evolution then followed the equation

$$C_{in}\frac{dV}{dt} = G_{in}(V_r - V) + G_{Nat}m^3h(E_{Na} - V) + G_{Nap}m_p^3s(V_{Na} - V) + G_{Kdr}n^3(E_K - V) + G_A m_A h_A(E_K - V) + I \quad (1),$$

where C_{in} was the input capacitance; G_{in} the input conductance; G_{Nat}, G_{Nap}, G_{Kdr} and G_A the maximal conductances of the aforementioned currents; m, m_p, n and m_A their activation variables; h the inactivation variable of I_{Nat}, s the slow inactivation variable of I_{Nap}, and m_A the inactivation variable of I_A. V_r is the baseline potential imposed by *ad hoc* current injection in current-clamp experiments; E_{Na} and E_K are the Nernst potentials of sodium and potassium ions, and I the injected current. All gating variables satisfied equations of the form:

$$\tau_x \frac{dx}{dt} = x_\infty(V) - x,$$

where the (in)activation curves were modeled by a sigmoid function of the form:

$$x_\infty = \frac{1}{1+\exp(-(V-V_x)/k_x)}$$

with k_x being positive for activation and negative for inactivation. The time constant τ_x was voltage-independent except for the inactivation variables h and s. The activation variable m_A of I_A was assumed to follow instantaneously voltage changes.

The effect of channel noise was investigated with a stochastic realization of the model, where channels kinetics were described by Markov-type models, assuming a unitary channel conductance of 10 pS for all channels.

Choice of model parameters

Most model parameters were chosen on the basis of experimental measurements performed in the present study or already reported [25]. Parameters that could not be constrained from our experimental data were chosen from an experimentally realistic range of values. V_r was set at -60 mV as in experiments (see ***table 1***). C_{in} (average 13.15 pF, 50% between 11.9 and 15.1 pF, only 18 cells out of 246 in the first quartile below 7.2 pF or in the fourth quartile above 19 pF) and G_{in} (50% of cells between 0.71 and 1.18 nS, only 7 out of 242 with input conductance above 2 nS) were not spread much in the cells recorded at E12.5, which showed that most embryonic $V1^R$ were of comparable size. Interestingly, C_{in} and G_{in} were not correlated, which indicated that the input conductance was determined by the density of leak channels rather than by the sheer size of the cell. Moreover, no correlation was observed between the passive properties and the firing pattern [25]. Therefore, we always set G_{in} and C_{in} to 1 nS and 13 pF in the model (except

737 in ***Figure 6—figure supplement 2***), close to the experimental medians (0.96 nS and 13.15
738 pF, respectively). The membrane time constant C_{in}/G_{in} was then equal to 13 ms, which
739 was also close to the experimental median (13.9 ms, N=241).
740 E_{Na} was set to 60 mV (see [25]). The activation curve of I_{Nap} was obtained by fitting
741 experimental data, leading to an average mid-activation of -36 mV and an average
742 steepness of 9.5 mV. The experimentally measured values of G_{Nap} were in the range 0-2.2
743 nS. We assumed that the activation curve of I_{Nat} was shifted rightward by 10 mV in
744 comparison to I_{Nap}. No experimental data was available for the inactivation of I_{Nat}. We
745 chose a mid-inactivation voltage V_h= -45 mV and a steepness k_h=-5 mV. We also assumed
746 that the activation time constant of both I_{Nat} and I_{Nap} was 1.5 ms, and that the
747 inactivation time constant was voltage-dependent:
748 $\tau_h(V) = 16.5 - 13.5\tanh((V+20)/15)$, decreasing by one order of magnitude (from 30
749 ms down to 3 ms) with the voltage increase. This enabled us to account for the shape of
750 the action potentials recorded in experiments, showing a slow rise time and rather long
751 duration. The conductance G_{Nat} was not measured experimentally. When choosing a
752 reasonable value of 20 nS for G_{Nat}, the model behaved very much as recorded embryonic
753 V1^R: with similar current threshold (typically 10-20 pA) and stable plateau potential
754 obtained for the largest values of G_{Nap}.
755 When taking into account slow inactivation of I_{Nap} (see ***Figure 8***), we chose V_s = -30 mV
756 for the mid-inactivation voltage and set the steepness k_s at -5 mV (as for the inactivation
757 of I_{Nat}). For simplicity, we assumed that the inactivation time constant was voltage-
758 independent and set it at a value of 2 s.
759 E_K was set to the experimentally measured value of -96 mV [25]. The activation
760 parameters of I_{Kdr} were obtained by fitting the experimental data: V_n = -20 mV, k_n = 15

mV, τ_n = 10 ms and an activation exponent of 3. The activation and inactivation properties of I_A were also chosen based on experimental measurements. Accordingly, V_{m_A} = -30 mV, k_{m_A} = -12 mV, V_{h_A} = -70 mV, k_{h_A} = -7 mV, and τ_{h_A}= 23 ms. When I_A was taken into account, we assumed that $G_A = G_{Kdr}$, consistently with experimental data (see ***Figure 6—figure supplement 1***).

Numerical simulations and dynamical systems analysis

We integrated numerically the deterministic model using the freeware XPP-Aut 8.0 (University of Pittsburgh; Pennsylvania; USA; RRID:SCR_001996) [85] and a standard fourth-order Runge-Kutta algorithm. XPP-Aut was also used to compute one-parameter and two-parameters bifurcation diagrams. The stochastic version of the model was also implemented in XPP-Aut and computed with a Gillespie's algorithm [86].

To investigate the dynamics of the model with slow inactivation of I_{Nap}, we relied on numerical simulations together with fast/slow dynamics analysis [87]. In this approach, one distinguishes slow dynamical variables (here only s) and fast dynamical variables. Slow variables vary little at the time scale of fast variables and may therefore be considered as constant parameters of the fast dynamics in first approximation. In contrast, slow variables are essentially sensitive to the time average of the fast variables, much more than to their instantaneous values. This separation of time scales allows one to conduct a phase plane analysis of the full dynamics.

Statistics

Samples sizes (n) were determined based on previous experience. The number of embryos (N) is indicated in the main text and figure captions. No power analysis was employed, but

785 sample sizes are comparable to those typically used in the field. All values were expressed
786 as mean with standard error of mean (SEM). Statistical significance was assessed by non-
787 parametric Kruskal-Wallis test with Dunn's post hoc test for multiple comparisons, Mann-
788 Whitney test for unpaired data or Wilcoxon matched pairs test for paired data using
789 GraphPad Prism 7.0e Software (USA). Significant changes in the proportions of firing
790 patterns with age were assessed by chi-square test for large sample and by Fisher's exact
791 test for small sample using GraphPad Prism 7.0e Software (GraphPad Software, USA;
792 RRID:SCR_002798). Significance was determined as $p<0.05$ (*), $p<0.01$ (**) or $p<0.001$
793 (***). The exact p value was mentioned in the result section or in the figure captions.

Acknowledgments

We thank Susanne Bolte, Jean-François Gilles and France Lam for assistance with confocal imaging (IBPS imaging facility) and IBPS rodent facility team for animal care and production. We thank University Paris Descartes for hosting Yulia Timofeeva as an invited professor. This work was supported by INSERM, CNRS, Sorbonne Université (Paris), Université de Bordeaux, Université Paris Descartes and Fondation pour la Recherche Médicale.

Additional information

Competing interests

The authors declare no competing interests

References

1. O'Donovan MJ. The origin of spontaneous activity in developing networks of the vertebrate nervous system. Curr Opin Neurobiol. 1999;9(1):94-104. PubMed PMID: 10072366.

2. Saint-Amant L. Development of motor rhythms in zebrafish embryos. Progress in brain research. 2010;187:47-61. doi: 10.1016/B978-0-444-53613-6.00004-6. PubMed PMID: 21111200.

3. Blankenship AG, Feller MB. Mechanisms underlying spontaneous patterned activity in developing neural circuits. Nature reviews Neuroscience. 2010;11(1):18-29. doi: 10.1038/nrn2759. PubMed PMID: 19953103; PubMed Central PMCID: PMC2902252.

4. Myers CP, Lewcock JW, Hanson MG, Gosgnach S, Aimone JB, Gage FH, et al. Cholinergic input is required during embryonic development to mediate proper assembly of spinal locomotor circuits. Neuron. 2005;46(1):37-49. Epub 2005/04/12. doi: S0896-6273(05)00165-0 [pii]
10.1016/j.neuron.2005.02.022. PubMed PMID: 15820692.

5. Milner LD, Landmesser LT. Cholinergic and GABAergic inputs drive patterned spontaneous motoneuron activity before target contact. J Neurosci. 1999;19(8):3007-22. PubMed PMID: 10191318.

6. Hanson MG, Landmesser LT. Characterization of the circuits that generate spontaneous episodes of activity in the early embryonic mouse spinal cord. J Neurosci. 2003;23(2):587-600. PubMed PMID: 12533619.

7. Momose-Sato Y, Sato K. Large-scale synchronized activity in the embryonic brainstem and spinal cord. Frontiers in cellular neuroscience. 2013;7:36. doi: 10.3389/fncel.2013.00036. PubMed PMID: 23596392; PubMed Central PMCID: PMC3625830.

8. Khazipov R, Luhmann HJ. Early patterns of electrical activity in the developing cerebral cortex of humans and rodents. Trends in neurosciences. 2006;29(7):414-8. doi: 10.1016/j.tins.2006.05.007. PubMed PMID: 16713634.

9. Allain AE, Le Corronc H, Delpy A, Cazenave W, Meyrand P, Legendre P, et al. Maturation of the GABAergic transmission in normal and pathologic motoneurons. Neural plasticity. 2011;2011:905624. doi: 10.1155/2011/905624. PubMed PMID: 21785735; PubMed Central PMCID: PMC3140191.

10. Branchereau P, Chapron J, Meyrand P. Descending 5-hydroxytryptamine raphe inputs repress the expression of serotonergic neurons and slow the maturation of inhibitory systems in mouse embryonic spinal cord. J Neurosci. 2002;22(7):2598-606. doi: 20026199. PubMed PMID: 11923425.

11. Yvert B, Branchereau P, Meyrand P. Multiple spontaneous rhythmic activity patterns generated by the embryonic mouse spinal cord occur within a specific developmental time window. Journal of neurophysiology. 2004;91(5):2101-9. doi: 10.1152/jn.01095.2003. PubMed PMID: 14724265.

12. Czarnecki A, Le Corronc H, Rigato C, Le Bras B, Couraud F, Scain AL, et al. Acetylcholine controls GABA-, glutamate-, and glycine-dependent giant depolarizing potentials that govern spontaneous motoneuron activity at the onset of synaptogenesis in the mouse embryonic spinal cord. J Neurosci. 2014;34(18):6389-404. doi: 10.1523/JNEUROSCI.2664-13.2014. PubMed PMID: 24790209.

13. Pun S, Sigrist M, Santos AF, Ruegg MA, Sanes JR, Jessell TM, et al. An intrinsic distinction in neuromuscular junction assembly and maintenance in different skeletal muscles. Neuron. 2002;34(3):357-70. doi: 10.1016/s0896-6273(02)00670-0. PubMed PMID: 11988168.

14. Angelim M, Maia L, Mouffle C, Ginhoux F, Low D, Amancio-Dos-Santos A, et al. Embryonic macrophages and microglia ablation alter the development of dorsal root ganglion sensory neurons in mouse embryos. Glia. 2018;66(11):2470-86. doi: 10.1002/glia.23499. PubMed PMID: 30252950.

15. Marmigere F, Ernfors P. Specification and connectivity of neuronal subtypes in the sensory lineage. Nature reviews Neuroscience. 2007;8(2):114-27. doi: 10.1038/nrn2057. PubMed PMID: 17237804.

16. Ozaki S, Snider WD. Initial trajectories of sensory axons toward laminar targets in the developing mouse spinal cord. The Journal of comparative neurology. 1997;380(2):215-29. PubMed PMID: 9100133.

17. Ballion B, Branchereau P, Chapron J, Viala D. Ontogeny of descending serotonergic innervation and evidence for intraspinal 5-HT neurons in the mouse spinal cord. Brain research Developmental brain research. 2002;137(1):81-8. doi: 10.1016/s0165-3806(02)00414-5. PubMed PMID: 12128257.

18. Moody WJ, Bosma MM. Ion channel development, spontaneous activity, and activity-dependent development in nerve and muscle cells. Physiological reviews. 2005;85(3):883-941. doi: 10.1152/physrev.00017.2004. PubMed PMID: 15987798.

873 19. Spitzer NC. Electrical activity in early neuronal development. Nature.
874 2006;444(7120):707-12. doi: 10.1038/nature05300. PubMed PMID: 17151658.
875 20. Katz LC, Shatz CJ. Synaptic activity and the construction of cortical circuits. Science.
876 1996;274(5290):1133-8. PubMed PMID: 8895456.
877 21. Hanson MG, Milner LD, Landmesser LT. Spontaneous rhythmic activity in early
878 chick spinal cord influences distinct motor axon pathfinding decisions. Brain Res Rev.
879 2008;57(1):77-85. Epub 2007/10/09. doi: S0165-0173(07)00127-0 [pii]
880 10.1016/j.brainresrev.2007.06.021. PubMed PMID: 17920131.
881 22. Hanson MG, Landmesser LT. Normal patterns of spontaneous activity are required
882 for correct motor axon guidance and the expression of specific guidance molecules. Neuron.
883 2004;43(5):687-701. doi: 10.1016/j.neuron.2004.08.018. PubMed PMID: 15339650.
884 23. Hanson MG, Landmesser LT. Increasing the frequency of spontaneous rhythmic
885 activity disrupts pool-specific axon fasciculation and pathfinding of embryonic spinal
886 motoneurons. J Neurosci. 2006;26(49):12769-80. doi: 10.1523/JNEUROSCI.4170-06.2006.
887 PubMed PMID: 17151280.
888 24. Benito-Gonzalez A, Alvarez FJ. Renshaw cells and Ia inhibitory interneurons are
889 generated at different times from p1 progenitors and differentiate shortly after exiting the
890 cell cycle. J Neurosci. 2012;32(4):1156-70. doi: 10.1523/JNEUROSCI.3630-12.2012.
891 PubMed PMID: 22279202; PubMed Central PMCID: PMC3276112.
892 25. Boeri J, Le Corronc H, Lejeune FX, Le Bras B, Mouffle C, Angelim M, et al.
893 Persistent Sodium Current Drives Excitability of Immature Renshaw Cells in Early
894 Embryonic Spinal Networks. J Neurosci. 2018;38(35):7667-82. doi:
895 10.1523/JNEUROSCI.3203-17.2018. PubMed PMID: 30012693.
896 26. Perry S, Gezelius H, Larhammar M, Hilscher MM, Lamotte d'Incamps B, Leao KE,
897 et al. Firing properties of Renshaw cells defined by Chrna2 are modulated by
898 hyperpolarizing and small conductance ion currents Ih and ISK. The European journal of
899 neuroscience. 2015;41(7):889-900. doi: 10.1111/ejn.12852. PubMed PMID: 25712471.
900 27. Bikoff JB, Gabitto MI, Rivard AF, Drobac E, Machado TA, Miri A, et al. Spinal
901 Inhibitory Interneuron Diversity Delineates Variant Motor Microcircuits. Cell.
902 2016;165(1):207-19. doi: 10.1016/j.cell.2016.01.027. PubMed PMID: 26949184; PubMed
903 Central PMCID: PMC4808435.
904 28. Delpy A, Allain AE, Meyrand P, Branchereau P. NKCC1 cotransporter inactivation
905 underlies embryonic development of chloride-mediated inhibition in mouse spinal

906 motoneuron. J Physiol. 2008;586(4):1059-75. doi: 10.1113/jphysiol.2007.146993. PubMed
907 PMID: 18096599; PubMed Central PMCID: PMC2375629.
908 29. Crill WE. Persistent sodium current in mammalian central neurons. Annual review of
909 physiology. 1996;58:349-62. doi: 10.1146/annurev.ph.58.030196.002025. PubMed PMID:
910 8815799.
911 30. Sillar KT, Simmers AJ, Wedderburn JF. The post-embryonic development of cell
912 properties and synaptic drive underlying locomotor rhythm generation in Xenopus larvae.
913 Proceedings Biological sciences. 1992;249(1324):65-70. doi: 10.1098/rspb.1992.0084.
914 PubMed PMID: 1359549.
915 31. Gao BX, Ziskind-Conhaim L. Development of ionic currents underlying changes in
916 action potential waveforms in rat spinal motoneurons. Journal of neurophysiology.
917 1998;80(6):3047-61. PubMed PMID: 9862905.
918 32. Gao H, Lu Y. Early development of intrinsic and synaptic properties of chicken
919 nucleus laminaris neurons. Neuroscience. 2008;153(1):131-43. doi:
920 10.1016/j.neuroscience.2008.01.059. PubMed PMID: 18355968.
921 33. McKay BE, Turner RW. Physiological and morphological development of the rat
922 cerebellar Purkinje cell. J Physiol. 2005;567(Pt 3):829-50. doi:
923 10.1113/jphysiol.2005.089383. PubMed PMID: 16002452; PubMed Central PMCID:
924 PMC1474219.
925 34. Liu X, Pfaff DW, Calderon DP, Tabansky I, Wang X, Wang Y, et al. Development
926 of Electrophysiological Properties of Nucleus Gigantocellularis Neurons Correlated with
927 Increased CNS Arousal. Developmental neuroscience. 2016;38(4):295-310. doi:
928 10.1159/000449035. PubMed PMID: 27788521; PubMed Central PMCID: PMC5127753.
929 35. Pineda R, Ribera A. Evolution of the Action Potential. In: Kaas JH, editor. Evolution
930 of Nervous Systems. 1: Elsevier Ltd; 2010. p. 211-38.
931 36. Coetzee WA, Amarillo Y, Chiu J, Chow A, Lau D, McCormack T, et al. Molecular
932 diversity of K+ channels. Annals of the New York Academy of Sciences. 1999;868:233-85.
933 doi: 10.1111/j.1749-6632.1999.tb11293.x. PubMed PMID: 10414301.
934 37. O'Leary T, Williams AH, Caplan JS, Marder E. Correlations in ion channel
935 expression emerge from homeostatic tuning rules. Proceedings of the National Academy of
936 Sciences of the United States of America. 2013;110(28):E2645-54. Epub 2013/06/27. doi:
937 10.1073/pnas.1309966110. PubMed PMID: 23798391; PubMed Central PMCID:
938 PMCPMC3710808.

939 38. Taylor AL, Goaillard JM, Marder E. How multiple conductances determine
940 electrophysiological properties in a multicompartment model. J Neurosci.
941 2009;29(17):5573-86. Epub 2009/05/01. doi: 10.1523/jneurosci.4438-08.2009. PubMed
942 PMID: 19403824; PubMed Central PMCID: PMCPMC2821064.
943 39. Alonso LM, Marder E. Visualization of currents in neural models with similar
944 behavior and different conductance densities. eLife. 2019;8. Epub 2019/02/01. doi:
945 10.7554/eLife.42722. PubMed PMID: 30702427; PubMed Central PMCID:
946 PMCPMC6395073.
947 40. Sigworth FJ, Sine SM. Data transformations for improved display and fitting of
948 single-channel dwell time histograms. Biophysical journal. 1987;52(6):1047-54. doi:
949 10.1016/S0006-3495(87)83298-8. PubMed PMID: 2447968; PubMed Central PMCID:
950 PMC1330104.
951 41. Ramoa AS, McCormick DA. Developmental changes in electrophysiological
952 properties of LGNd neurons during reorganization of retinogeniculate connections. J
953 Neurosci. 1994;14(4):2089-97. PubMed PMID: 8158259; PubMed Central PMCID:
954 PMC6577110.
955 42. Belleau ML, Warren RA. Postnatal development of electrophysiological properties
956 of nucleus accumbens neurons. Journal of neurophysiology. 2000;84(5):2204-16. doi:
957 10.1152/jn.2000.84.5.2204. PubMed PMID: 11067966.
958 43. Picken Bahrey HL, Moody WJ. Early development of voltage-gated ion currents and
959 firing properties in neurons of the mouse cerebral cortex. Journal of neurophysiology.
960 2003;89(4):1761-73. doi: 10.1152/jn.00972.2002. PubMed PMID: 12611962.
961 44. Tong H, McDearmid JR. Pacemaker and plateau potentials shape output of a
962 developing locomotor network. Current biology : CB. 2012;22(24):2285-93. doi:
963 10.1016/j.cub.2012.10.025. PubMed PMID: 23142042; PubMed Central PMCID:
964 PMC3525839.
965 45. Alvarez FJ, Benito-Gonzalez A, Siembab VC. Principles of interneuron development
966 learned from Renshaw cells and the motoneuron recurrent inhibitory circuit. Annals of the
967 New York Academy of Sciences. 2013;1279:22-31. doi: 10.1111/nyas.12084. PubMed
968 PMID: 23530999; PubMed Central PMCID: PMC3870136.
969 46. Allain AE, Segu L, Meyrand P, Branchereau P. Serotonin controls the maturation of
970 the GABA phenotype in the ventral spinal cord via 5-HT1b receptors. Annals of the New
971 York Academy of Sciences. 2010;1198:208-19. doi: 10.1111/j.1749-6632.2010.05433.x.
972 PubMed PMID: 20536936.

973 47. Branchereau P, Morin D, Bonnot A, Ballion B, Chapron J, Viala D. Development of
974 lumbar rhythmic networks: from embryonic to neonate locomotor-like patterns in the mouse.
975 Brain research bulletin. 2000;53(5):711-8. doi: 10.1016/s0361-9230(00)00403-2. PubMed
976 PMID: 11165805.
977 48. Spitzer NC, Vincent A, Lautermilch NJ. Differentiation of electrical excitability in
978 motoneurons. Brain research bulletin. 2000;53(5):547-52. PubMed PMID: 11165790.
979 49. Prasad T, Wang X, Gray PA, Weiner JA. A differential developmental pattern of
980 spinal interneuron apoptosis during synaptogenesis: insights from genetic analyses of the
981 protocadherin-gamma gene cluster. Development. 2008;135(24):4153-64. doi:
982 10.1242/dev.026807. PubMed PMID: 19029045; PubMed Central PMCID: PMC2755264.
983 50. Taddese A, Bean BP. Subthreshold sodium current from rapidly inactivating sodium
984 channels drives spontaneous firing of tuberomammillary neurons. Neuron. 2002;33(4):587-
985 600. doi: 10.1016/s0896-6273(02)00574-3. PubMed PMID: 11856532.
986 51. Kuo JJ, Lee RH, Zhang L, Heckman CJ. Essential role of the persistent sodium
987 current in spike initiation during slowly rising inputs in mouse spinal neurones. J Physiol.
988 2006;574(Pt 3):819-34. doi: 10.1113/jphysiol.2006.107094. PubMed PMID: 16728453;
989 PubMed Central PMCID: PMC1817738.
990 52. Ori H, Marder E, Marom S. Cellular function given parametric variation in the
991 Hodgkin and Huxley model of excitability. Proceedings of the National Academy of
992 Sciences of the United States of America. 2018;115(35):E8211-E8. Epub 2018/08/17. doi:
993 10.1073/pnas.1808552115. PubMed PMID: 30111538; PubMed Central PMCID:
994 PMCPMC6126753.
995 53. Teka W, Tsaneva-Atanasova K, Bertram R, Tabak J. From plateau to pseudo-plateau
996 bursting: making the transition. Bulletin of mathematical biology. 2011;73(6):1292-311. doi:
997 10.1007/s11538-010-9559-7. PubMed PMID: 20658200; PubMed Central PMCID:
998 PMC3152987.
999 54. Bertram R, Butte MJ, Kiemel T, Sherman A. Topological and phenomenological
1000 classification of bursting oscillations. Bulletin of mathematical biology. 1995;57(3):413-39.
1001 doi: 10.1007/BF02460633. PubMed PMID: 7728115.
1002 55. Izhikevich EM. Neural excitability, spiking and bursting. Int J Bifurcation Chaos.
1003 2000;10(06):1171-266.
1004 56. Borisyuk A, Rinzel J. Understanding neuronal dynamics by geometrical dissection of
1005 minimal models. In: Chow C, Gutkin B, Hansel D, Meunier C, Dalibard J, editors. Models

and Methods in Neurophysics. Proc Les Houches Summer School 2003, (Session LXXX): Elsevier; 2005. p. 19-72.

57. Rinzel J. Bursting oscillations in an excitable membrane model. In: Sleeman B, Jarvis R, editors. Ordinary and Partial Differential Equations Lecture Notes in Mathematics. 1151. Berlin, Heidelberg: Springer; 1985. p. 304–16.

58. Stern JV, Osinga HM, LeBeau A, Sherman A. Resetting behavior in a model of bursting in secretory pituitary cells: distinguishing plateaus from pseudo-plateaus. Bulletin of mathematical biology. 2008;70(1):68-88. doi: 10.1007/s11538-007-9241-x. PubMed PMID: 17703340.

59. Osinga HM, Tsaneva-Atanasova KT. Dynamics of plateau bursting depending on the location of its equilibrium. Journal of neuroendocrinology. 2010;22(12):1301-14. doi: 10.1111/j.1365-2826.2010.02083.x. PubMed PMID: 20955345.

60. Osinga HM, Sherman A, Tsaneva-Atanasova K. Cross-Currents between Biology and Mathematics: The Codimension of Pseudo-Plateau Bursting. Discrete and continuous dynamical systems Series A. 2012;32(8):2853-77. doi: 10.3934/dcds.2012.32.2853. PubMed PMID: 22984340; PubMed Central PMCID: PMC3439852.

61. Golomb D, Yue C, Yaari Y. Contribution of persistent Na+ current and M-type K+ current to somatic bursting in CA1 pyramidal cells: combined experimental and modeling study. Journal of neurophysiology. 2006;96(4):1912-26. Epub 2006/06/30. doi: 10.1152/jn.00205.2006. PubMed PMID: 16807352.

62. Del Negro CA, Koshiya N, Butera RJ, Jr., Smith JC. Persistent sodium current, membrane properties and bursting behavior of pre-bötzinger complex inspiratory neurons in vitro. Journal of neurophysiology. 2002;88(5):2242-50. Epub 2002/11/09. doi: 10.1152/jn.00081.2002. PubMed PMID: 12424266.

63. Rybak IA, Shevtsova NA, Ptak K, McCrimmon DR. Intrinsic bursting activity in the pre-Bötzinger complex: role of persistent sodium and potassium currents. Biological cybernetics. 2004;90(1):59-74. Epub 2004/02/06. doi: 10.1007/s00422-003-0447-1. PubMed PMID: 14762725.

64. Izhikevich EM. Subcritical Elliptic Bursting of Bautin Type. SIAM Journal on Applied Mathematics. 2000;60(2):503-35. doi: https://doi.org/10.1137/S003613999833263X.

65. Su J, Rubin J, Terman D. Effects of noise on elliptic bursters. Nonlinearity. 2004;17(1):133-57. doi: https://doi.org/10.1088/0951-7715/17/1/009.

66. Stam FJ, Hendricks TJ, Zhang J, Geiman EJ, Francius C, Labosky PA, et al. Renshaw cell interneuron specialization is controlled by a temporally restricted transcription factor program. Development. 2012;139(1):179-90. doi: 10.1242/dev.071134. PubMed PMID: 22115757; PubMed Central PMCID: PMC3231776.

67. Eccles JC, Fatt P, Landgren S. The inhibitory pathway to motoneurones. Progress in neurobiology. 1956;(2):72-82. PubMed PMID: 13441782.

68. Vinay L, Brocard F, Clarac F. Differential maturation of motoneurons innervating ankle flexor and extensor muscles in the neonatal rat. The European journal of neuroscience. 2000;12(12):4562-6. doi: 10.1046/j.0953-816x.2000.01321.x. PubMed PMID: 11122369.

69. Durand J, Filipchuk A, Pambo-Pambo A, Amendola J, Borisovna Kulagina I, Gueritaud JP. Developing electrical properties of postnatal mouse lumbar motoneurons. Frontiers in cellular neuroscience. 2015;9:349. doi: 10.3389/fncel.2015.00349. PubMed PMID: 26388736; PubMed Central PMCID: PMC4557103.

70. Marcotti W, Johnson SL, Holley MC, Kros CJ. Developmental changes in the expression of potassium currents of embryonic, neonatal and mature mouse inner hair cells. J Physiol. 2003;548(Pt 2):383-400. doi: 10.1113/jphysiol.2002.034801. PubMed PMID: 12588897; PubMed Central PMCID: PMC2342842.

71. Marcotti W, Johnson SL, Rusch A, Kros CJ. Sodium and calcium currents shape action potentials in immature mouse inner hair cells. J Physiol. 2003;552(Pt 3):743-61. doi: 10.1113/jphysiol.2003.043612. PubMed PMID: 12937295; PubMed Central PMCID: PMC2343463.

72. Sontheimer H, Trotter J, Schachner M, Kettenmann H. Channel expression correlates with differentiation stage during the development of oligodendrocytes from their precursor cells in culture. Neuron. 1989;2(2):1135-45. doi: 10.1016/0896-6273(89)90180-3. PubMed PMID: 2560386.

73. Allain AE, Bairi A, Meyrand P, Branchereau P. Ontogenic changes of the GABAergic system in the embryonic mouse spinal cord. Brain research. 2004;1000(1-2):134-47. doi: 10.1016/j.brainres.2003.11.071. PubMed PMID: 15053961.

74. Sapir T, Geiman EJ, Wang Z, Velasquez T, Mitsui S, Yoshihara Y, et al. Pax6 and engrailed 1 regulate two distinct aspects of renshaw cell development. J Neurosci. 2004;24(5):1255-64. doi: 10.1523/JNEUROSCI.3187-03.2004. PubMed PMID: 14762144; PubMed Central PMCID: PMC2997484.

75. Henley J, Poo MM. Guiding neuronal growth cones using Ca2+ signals. Trends in cell biology. 2004;14(6):320-30. doi: 10.1016/j.tcb.2004.04.006. PubMed PMID: 15183189; PubMed Central PMCID: PMC3115711.

76. Tsaneva-Atanasova K, Osinga HM, Riess T, Sherman A. Full system bifurcation analysis of endocrine bursting models. Journal of theoretical biology. 2010;264(4):1133-46. doi: 10.1016/j.jtbi.2010.03.030. PubMed PMID: 20307553; PubMed Central PMCID: PMC3128456.

77. Tagliavini A, Tabak J, Bertram R, Pedersen MG. Is bursting more effective than spiking in evoking pituitary hormone secretion? A spatiotemporal simulation study of calcium and granule dynamics. American journal of physiology Endocrinology and metabolism. 2016;310(7):E515-25. doi: 10.1152/ajpendo.00500.2015. PubMed PMID: 26786781.

78. Oster A, Faure P, Gutkin BS. Mechanisms for multiple activity modes of VTA dopamine neurons. Frontiers in computational neuroscience. 2015;9:95. doi: 10.3389/fncom.2015.00095. PubMed PMID: 26283955; PubMed Central PMCID: PMC4516885.

79. Chevalier M, Toporikova N, Simmers J, Thoby-Brisson M. Development of pacemaker properties and rhythmogenic mechanisms in the mouse embryonic respiratory network. eLife. 2016;5. doi: 10.7554/eLife.16125. PubMed PMID: 27434668; PubMed Central PMCID: PMC4990420.

80. Kole MH, Stuart GJ. Signal processing in the axon initial segment. Neuron. 2012;73(2):235-47. doi: 10.1016/j.neuron.2012.01.007. PubMed PMID: 22284179.

81. Tamamaki N, Yanagawa Y, Tomioka R, Miyazaki J, Obata K, Kaneko T. Green fluorescent protein expression and colocalization with calretinin, parvalbumin, and somatostatin in the GAD67-GFP knock-in mouse. The Journal of comparative neurology. 2003;467(1):60-79. doi: 10.1002/cne.10905. PubMed PMID: 14574680.

82. Scain AL, Le Corronc H, Allain AE, Muller E, Rigo JM, Meyrand P, et al. Glycine release from radial cells modulates the spontaneous activity and its propagation during early spinal cord development. J Neurosci. 2010;30(1):390-403. Epub 2010/01/08. doi: 30/1/390 [pii]

10.1523/JNEUROSCI.2115-09.2010. PubMed PMID: 20053920.

83. Huang H, Trussell LO. Control of presynaptic function by a persistent Na(+) current. Neuron. 2008;60(6):975-9. doi: 10.1016/j.neuron.2008.10.052. PubMed PMID: 19109905; PubMed Central PMCID: PMC2657474.

84. Rousseeuw PJ. Silhouettes - a Graphical Aid to the Interpretation and Validation of Cluster-Analysis. J Comput Appl Math. 1987;20:53-65. doi: Doi 10.1016/0377-0427(87)90125-7. PubMed PMID: WOS:A1987L111800005.

85. Ermentrout B. Simulating, Analyzing, and Animating Dynamical Systems: A Guide to XPPAUT for Researchers and Students. Philadelphia: Society for Industrial and Applied Mathematics; 2002.

86. Gillespie DT. A general method for numerically simulating the stochastic time evolution of coupled chemical reactions. Journal of Computational Physics. 1976;22(4):403-34. doi: https://doi.org/10.1016/0021-9991(76)90041-3.

87. Witelski T, Bowen M. Fast/slow Dynamical Systems. In: Methods of Mathematical Modelling: Springer, Cham; 2015.

Figure captions

Figure 1. G_{Kdr} and G_{Nap} in embryonic V1^R at E12.5 and E14.5

(A) Representative traces of voltage responses showing single-spiking activity in E12.5 SS V1^R (A1), repetitive action potential firing in RS V1^R (A2), Mixed of plateau potential activity and repetitive action potential firing in ME V1^R (A3) and plateau potential activity in PP V1^R (A4). (B) Representative examples of the total outward K^+ currents (IKv total) obtained from V_H = -100 mV (left traces), of I_{Kdr} (V_H = -30 mV, middle traces) and of isolated I_A (left traces) recorded at E12.5 in SS V1^R (B1), RS V1^R (B2), ME V1^R (B3) and PP V1^R (B4). Voltage-dependent potassium currents were evoked in response to 10 mV membrane potential steps (200 ms) from -100 or from -30 mV to +40 mV (10 s interval between pulses). V1^R were voltage clamped at V_H = -60 mV. A prepulse of -40 mV (300 ms) was applied to activate both I_A and I_{Kdr}. I_{Kdr} was isolated by applying a prepulse of 30 mV (300 ms) to inactivate I_A (B1 insert). I_A was isolated by subtracting step-by-step the currents obtained using a pre-pulse of 30 mV (V_H = - 30 mV) from the currents obtained using a pre-pulse of -40 mV (V_H = -100 mV). (C) Current-voltage relationship ($I-V$ curves) of I_{Kdr} (filled circles) and of I_A (open circles) recorded in SS V1^R (C1), RS V1^R (C2), ME V1^R (C3) and PP V1^R (C4). $I-V$ curves were obtained from currents shown in B1, B2, B3 and B4. Note that $I-V$ curves are similar between SS V1^R, RS V1^R, ME V1^R and PP V1^R. (D) Bar graph showing maximal G_{Kdr} value (Max G_{Kdr}) in SS V1^R at E12.5 (n = 9; N = 9; gray bar) and at E14.5 (n = 10; N = 10 gray bar), and in RS V1^R (n = 7; N = 7; red bar), ME V1^R (n = 3; N = 3 purple bar) and PP V1^R at E12.5 (n = 7; N = 7 blue bar). G_{Kdr} was calculated from I_{Kdr} at V_H = + 20 mV, assuming a K^+ equilibrium potential of -96 mV. There is no significant difference in G_{Kdr} between SS V1^R and RS V1^R, while G_{Kdr} is significantly smaller in PP V1^R as compared to SS V1^R and RS V1^R. G_{Kdr} was significantly higher in SS V1^R at E14.5 than in SS

1143 $V1^R$, RS $V1^R$ and PP $V1^R$ at E12.5. (Kruskall-Wallis test $P < 0.0001$; SS $V1^R$ versus RS $V1^R$ at
1144 E12.5, $P = 0.5864$; SS $V1^R$ versus PP $V1^R$ at E12.5, $P = 0.0243$; RS $V1^R$ versus PP $V1^R$ at E12.5,
1145 $P = 0.0086$; E14.5 SS $V1^R$ versus E12.5 SS $V1^R$, $P = 0.0048$; E14.5 SS $V1^R$ versus E12.5 RS $V1^R$,
1146 $P = 0.0384$, E14.5 SS $V1^R$ versus E12.5 PP $V1^R$, $P < 0.0001$). The increase in G_{Kdr} between
1147 E12.5 and E14.5 is likely to be due to the increase in neuronal size (input capacitance;
1148 Figure 2A). Indeed, there was no significant difference (Mann Whitney test, $P = 0.133$)
1149 in G_{Kdr} density between SS $V1^R$ at E12.5 (n = 9; N = 9 gray bar) and at E14.5 (n = 10; N = 10
1150 gray bar). (E) Bar graph showing the maximal G_{Nap} value ($\mathrm{Max}\ G_{Nap}$) in SS $V1^R$ at E12.5 (n =
1151 9; N = 9 gray bar) and E14.5 (n = 10; N = 10 gray bar), and in RS $V1^R$ (n = 8; N = 8 red bar),
1152 ME $V1^R$ (n = 3; N = 3 purple bar) and PP $V1^R$ (n = 6; N = 6 blue bar) at E12.5. Max G_{Nap} was
1153 calculated from maximal I_{Nap} value measured on current evoked by assuming a Na^+
1154 equilibrium potential of +60 mV. There was no difference in G_{Nap} between RS $V1^R$ and PP
1155 $V1^R$. On the contrary, G_{Nap} measured in SS $V1^R$ at E12.5 or at E14.5 was significantly
1156 smaller as compared to G_{Nap} measured at E12.5 in RS $V1^R$ or in PP $V1^R$. G_{Nap} measured at
1157 E12.5 and E14.5 in SS $V1^R$ were not significantly different (Kruskall-Wallis test $P < 0.0001$;
1158 E12.5 SS $V1^R$ versus E12.5 RS $V1^R$, $P = 0.0034$; E12.5 SS $V1^R$ versus E12.5 PP $V1^R$, $P = 0.0006$;
1159 E12.5 RS $V1^R$ versus E12.5 PP $V1^R$, $P = 0.5494$; E14.5 SS $V1^R$ versus E12.5 SS $V1^R$, $P = 0.5896$;
1160 E14.5 SS $V1^R$ versus E12.5 RS $V1^R$, $P = 0.0005$; E14.5 SS $V1^R$ versus E12.5 PP $V1^R$, $P < 0.0001$).
1161 (F) Histograms showing the G_{Nap} / G_{Kdr} ratio in SS $V1^R$ at E12.5 (n = 9; gray bar) and E14.5
1162 (n = 10; green bar) and in RS $V1^R$ (n = 8; red bar), ME $V1^R$ (n = 3; purple bar) and PP $V1^R$ (n =
1163 6; blue bar) at E12.5. Note that the G_{Nap} / G_{Kdr} ratio differs significantly between SS $V1^R$,
1164 RS $V1^R$ and PP $V1^R$ at E12.5, while it is not different between SS $V1^R$ recorded at E12.5 and
1165 at E14.5 (Kruskall-Wallis test $P < 0.0001$; SS $V1^R$ versus RS $V1^R$ at E12.5, $P = 0.0367$; SS $V1^R$
1166 versus PP $V1^R$ at E12.5, $P < 0.0001$; RS $V1^R$ versus PP $V1^R$ at E12.5, $P = 0.0159$; E14.5 SS $V1^R$

versus E12.5 SS $V1^R$, *P* = 0.2319; E14.5 SS $V1^R$ versus E12.5 RS $V1^R$, *P* = 0.0017; E14.5 SS $V1^R$ versus E12.5 PP $V1^R$ *P* < 0.0001). Data shown in A and B were used to calculate G_{Nap} / G_{Kdr} ratio shown in C. (*P < 0.05, ** P < 0.01, *** P < 0.001).

Figure 2. Increasing 4-AP concentration changed the firing pattern of single spiking embryonic $V1^R$ recorded at E12.5

The firing pattern of embryonic $V1^R$ was evoked by 2 s suprathreshold depolarizing current steps. (A) Representative traces showing examples of the effect of increasing concentration of 4-AP (from 3 to 300 µM) on the firing pattern of a SS $V1^R$ recorded at E12.5. Note that in A1, increasing 4-AP concentration converted single spiking (gray trace) to repetitive spiking (red trace), repetitive spiking to a mixed event pattern (purple trace) and mixed events to plateau potential (blue trace). (A2) Example of SS $V1^R$ in which increasing 4-AP concentration converted single spiking to repetitive spiking only. (A3) Bar plots showing the change in the firing pattern of SS $V1^R$ according to 4-AP concentrations (control n = 10; N = 10, 3 µM 4-AP n = 8; N = 8, 10 µM 4-AP n = 10; N = 10, 30 µM 4-AP n = 10; N = 10, 100 µM 4-AP n = 10; N = 10, 300 µM 4-AP n = 8; N = 8). (B) Representative traces showing the effect of 0.5 µM TTX on a plateau potential evoked in a SS $V1^R$ in the presence of 300 µM 4-AP. (C) Representative traces showing the effect of 0.5 µM TTX on repetitive AP firing evoked in a SS $V1^R$ in the presence of 300 µM 4-AP. In both cases, the application of TTX fully blocked the responses evoked in the presence of 4-AP, indicating that they were underlain by the activation of voltage-gated Na^+ channels.

Figure 3. Cluster analysis of $V1^R$ firing pattern at E12.5

1190 (A, inserts) Cluster analysis of embryonic $V1^R$ firing pattern was performed using three
1191 parameters that describe the firing pattern during a 2 s suprathreshold depolarizing pulses:
1192 the mean of the half-amplitude event duration (mean ½Ad), the coefficient of variation of
1193 ½ Ad (CV ½Ad) allowing to quantify the AP variation within a train (CV was set to 0 when
1194 the number of spikes evoked by a depolarizing pulse was ≤ 3) and the duration ratio ddr =
1195 Σ½ Ad/Pw, obtained by dividing the sum of ½ Ad by the pulse duration Pw, that indicates
1196 the total time spent in the depolarized state. For example, ddr = 1 when a plateau potential
1197 lasts as long as the depolarizing pulse. Conversely, its value is low when the depolarizing
1198 pulse evokes a single AP only. (A) Dendrogram for complete linkage hierarchical clustering
1199 of 164 embryonic $V1^R$ (N = 140) according to the values of log mean ½Ad, of CV ½Ad and of
1200 log ddr. The colored matrix below the dendrogram shows the variations of these three
1201 parameters for all the cells in the clusters (colored trees) extracted from the dendrogram.
1202 (B) The number of clusters was determined by analyzing the distribution of silhouette
1203 width values (see Material and Methods). The boxplots show the distribution of silhouette
1204 width values when the number of clusters k varies from 2 to 12. The mean silhouette width
1205 values (red diamond shaped points) attained their maximum when the estimated cluster
1206 number was 5. (C) 3D plot showing cluster distribution of embryonic $V1^R$ according to log
1207 mean ½Ad, CV ½Ad and log ddr. Each cluster corresponds to a particular firing pattern as
1208 illustrated in D. $V1^R$ that cannot sustain repetitive firing of APs (1 to 3 AP/pulse only, gray,
1209 Single spiking, SS), $V1^R$ that can fire tonically (red, Repetitive spiking, RS), $V1^R$ with a firing
1210 pattern characterized by a mix of APs and relatively short plateau potentials (dark purple,
1211 Mixed event short PP, ME short PP), $V1^R$ with a firing pattern characterized by a mix of APs
1212 and relatively long plateau potentials (light purple, Mixed event long PP, ME long PP) and
1213 $V1^R$ with evoked plateau potentials only (blue, Plateau potential, PP). The arrow in C

indicates 3 misclassified $V1^R$ that could not sustain repetitive firing although they were assigned to the cluster of repetitively firing $V1^R$ (see text).

Figure 4. Developmental changes of embryonic $V1^R$ firing patterns from E11.5 to E16.5

(A1) Graph showing how the input capacitance C_{in} of $V1^R$ changes with embryonic age. C_{in} significantly increased between E12.5 or E13.5 and E14.5 (Kruskall-Wallis test $P < 0.0001$; E12.5 versus E11.5 $P = 0.258$, E12.5 versus E13.5 $P = 0.904$, E12.5 versus E14.5 $P < 0.0001$, E12.5 versus E15.5 $P < 0.0001$, E12.5 versus E16.5 $P < 0.0001$, E13.5 versus E14.5 $P < 0.0001$, E13.5 versus E15.5 $P < 0.0001$, E13.5 versus E16.5 $P < 0.0001$; E11.5 n = 31; N = 27, E12.5 n = 267; N = 152, E13.5 n = 43; N = 40, E14.5 n = 61; N = 49, E15.5 n = 16; N = 4, E16.5 n = 30; N = 9). (A2) Graph showing how the input resistance R_{in} of $V1^R$ changes with embryonic age. R_{in} significantly decreased between E12.5 or E14.5 and E15.5 (Kruskall-Wallis test $P < 0.0001$; E12.5 versus E11.5 $P > 0.999$, E12.5 versus E13.5 $P = 0.724$, E12.5 versus E14.5 $P > 0.999$, E12.5 versus E15.5 $P = 0.0004$, E12.5 versus E16.5 $P = 0.0005$, E14.5 versus E15.5 $P = 0.0019$, E14.5 versus E16.5 $P < 0.0058$; E11.5 n = 31, E12.5 n = 261; N = 146, E13.5 n = 43; N = 40, E14.5 n = 60; N = 48, E15.5 n = 16; N = 4, E16.5 n = 30; N = 9). (A3) Graph showing how the threshold of regenerative events (APs and plateau potentials) of $V1^R$ changes with embryonic age. The average threshold became significantly more hyperpolarized after E12.5 (Kruskall-Wallis test $P < 0.0001$; E12.5 versus E11.5 $P = 0.676$, E12.5 versus E13.5 $P = 0.0039$, E12.5 versus E14.5 $P < 0.0001$, E12.5 versus E15.5 $P < 0.0001$, E12.5 versus E16.5 $P < 0.0001$, E13.5 versus E14.5 $P > 0.999$, E13.5 versus E15.5 $P = 0.1398$, E13.5 versus E16.5 $P = 0.0013$; E14.5 versus E15.5 $P > 0.999$, E14.5 versus E16.5 $P = 0.0634$, E15.5 versus E16.5 $P > 0.999$; E11.5 n = 20; N = 16, E12.5 n = 162; N = 139, E13.5 n = 31; N = 28, E14.5 n = 30; N = 26, E15.5 n = 16; N = 4, E16.5 n = 30; N = 9). Yellow and purple bars below the graphs

indicate the two important phases of the functional development of spinal cord networks. The first one is characterized by synchronized neuronal activity (SNA) and the second one is characterized by the emergence of a locomotor-like activity (see text). Note that changes in C_{in} and R_{in} occurred at the end of the first developmental phase. (*P < 0.05, ** P < 0.01, *** P < 0.001; control, E12.5). The intrinsic activation properties were analyzed using 2 s suprathreshold depolarizing current steps. (B) Representative traces of voltage responses showing Single Spiking (SS) $V1^R$ (gray), Repetitive Spiking (RS) $V1^R$ (red), ME $V1^R$ (purple) and Plateau Potential (PP) $V1^R$ (blue) at E11.5 (B1), E13.5 (B2), E14.5 (B3) E15.5 (B4) and E16.5 (B5). (C) Bar graph showing how the proportions of the different firing patterns change from E11.5 to E16.5 (E11.5 n = 22; N = 18, E12.5 n = 163; N = 140, E13.5 n = 32; N = 29, E14.5 n = 57; N = 45, E15.5 n = 15; N = 4, E16.5 n = 28; N = 9). Yellow and purple bars below the graphs indicate the first and the second phase of functional embryonic spinal cord networks. The proportions of the different firing patterns significantly changed between E11.5 to E12.5 (Fisher's exact test, P = 0.0052) with a significant increase in the proportion of RS $V1^R$ (Fisher's exact test, P = 0.0336) and a significant decrease in the proportion of ME $V1^R$ (Fisher's exact test, P = 0.01071) at E12.5. Only two firing patterns (SS and RS) were observed after E13.5 and most embryonic $V1^R$ lost their ability to sustain tonic firing after E13.5. However, at E16.5 the proportion of RS $V1^R$ significantly increased at the expense of SS $V1^R$ when compared to E14.5 (Fisher's exact test, P = 0.0112), indicating that embryonic $V1^R$ began to recover the ability to sustain tonic firing after E15.5.

Figure 5. **Activated caspase-3 is not observed in embryonic $V1^R$ at E14.5**

Representative confocal image of the ventral part of an isolated lumbar spinal cord of E14.5 GAD67-eGFP mouse embryo showing immunostainings using antibodies against

eGFP (A), FoxD3 (B) and activated Caspase 3 (aCaspace 3) (C). (D) Superimposition of the three stainings shows that embryonic $V1^R$ (eGFP+ and FoxD3+) were not aCaspase 3 immunoreactive. (A1, B1, C1 and D1). Enlarged images from A, B and C showing that aCaspase 3 staining is localized in areas where eGFP and Foxd3 staining were absent. (A2, B2, C2 and D2) Enlarged images from A, B and C showing that aCaspase 3 staining is absent in the area where $V1^R$ (eGFP+ and FoxD3+) are located. aCaspase 3 staining that did not co-localize with GAD67eGFP likely indicates MN developmental cell death.

Figure 6. 600 μM 4-AP changed the firing pattern of single spiking embryonic $V1^R$ recorded at E14.5

The firing pattern of embryonic $V1^R$ was evoked by 2 s suprathreshold depolarizing current steps. (A) Representative traces showing the effect of 4-AP application (600 μM) on the firing pattern of single spiking (SS) $V1^R$ recorded at E14.5. Note that the applications of 600 μM 4-AP evoked either a plateau potential (A1) or repetitive spiking (A2), both fully blocked by TTX. (B) Bar plots showing the proportions of the different firing patterns observed in the presence of 600 μM 4-AP versus control recorded in SS $V1^R$ at E14.5 (n = 14; N = 14). Single Spiking (SS) $V1^R$ (gray), Repetitive Spiking (RS) $V1^R$ (red), Mixed Events (ME) $V1^R$ (purple), Plateau Potential (PP) $V1^R$ (blue).

Figure 7. Embryonic $V1^R$ firing patterns predicted by computational modeling

(A) Firing patterns of 27 recorded cells, in which both G_{Nap} and G_{Kdr} were measured. Gray: SS, red: RS, blue: PP. The three purple points located at the boundary between the RS and PP regions correspond to mixed events (ME) where plateau potentials alternate with spiking episodes. Note that no cell exhibited low values of both G_{Nap} and G_{Kdr} (lower left),

or large values of both conductances (upper right). (B) Bifurcation diagram of the deterministic model when G_{Kdr} is kept fixed to 2.5 nS or 10 nS while G_{Nap} is varied between 0 and 2.5 nS. G_{in} = 1 nS and I = 20 pA. For G_{Kdr} = 10 nS (i.e., in the top experimental range), the red curves indicate the maximal and minimal voltages achieved on the stable limit cycle associated with repetitive firing (solid lines) and on the unstable limit cycle (dashed lines). The fixed point of the model is indicated by a gray solid line when it corresponds to the stable quiescent state, a gray dashed line when it is unstable and a solid blue line when it corresponds to a stable plateau potential. The two HB corresponding to the change of stability of the quiescence state (HB_1, G_{Nap}= 0.81 nS) and of the voltage plateau (HB_2, G_{Nap}= 2.13 nS) are indicated, as well as the two SN bifurcations of limit cycles associated with the onset (SN_1, $G_{Nap} = 0.65$ nS) and offset (SN_2, G_{Nap}= 2.42 nS) of repetitive spiking as G_{Nap} is increased. For G_{Kdr} = 2.5 nS, the model does not display repetitive firing; it possesses a unique fixed point, which is always stable (blue-gray curve). The transition from quiescence to plateau is gradual with no intervening bifurcation. Representative voltage traces of the three different activity patterns are shown: single spiking in response to a 2 s current pulse (gray, G_{Nap} = 0.2 nS, G_{Kdr} = 10 nS), repetitive spiking (red, G_{Nap} = 1.2 nS, G_{Kdr} = 10 nS) and plateau potential (blue, G_{Nap} = 1.2 nS, G_{Kdr} = 2.5 nS). Note that the plateau never outlasts the current pulse. (C) Bifurcation diagram when G_{Nap} is kept fixed at 1.2 nS and G_{Kdr} is varied between 0 and 25 nS (I = 20 pA). Same conventions as in B. Plateau potential is stable until the subcritical Hopf bifurcation HB_2 (G_{Kdr} = 6.34 nS) is reached, repetitive firing can be observed between SN_2 (G_{Kdr} = 5.93 nS) and SN_1 (G_{Kdr} = 22.65 nS). The quiescent state is stable from point HB_1 ($G_{Kdr} = 17.59$ nS) onward. (D) Two-parameters bifurcation diagram of the model in the G_{Nap} - G_{Kdr} plane (I = 20 pA). The black merged curves indicate the bifurcations HB_1 and HB_2. The red curves

indicate the SN bifurcations of limit cycles SN_1 and SN_2. The shaded area indicates the region where repetitive firing can occur. The oblique lines through the points labeled 1, 2 and 3, the same as in B, correspond to three different values of the ratio G_{Nap}/G_{Kdr} : 0.02 (gray), 0.12 (red) and 0.48 (blue). Voltage traces on the right display the response to a 2 s current pulse when channel noise is taken into account for the three regimes: quiescence (top, gray trace and dot in the diagram), repetitive firing (middle, red) and plateau potential (bottom, blue). They correspond to the three deterministic voltage traces shown in B. Note that the one-parameter bifurcation diagrams shown in B correspond to horizontal lines through points 1 and 2 (G_{Kdr} = 10 nS) and through point 3 (G_{Kdr} = 2.5 nS), respectively. The bifurcation diagram in C corresponds to a vertical line through point 2 and 3 (G_{Nap} = 1.2 nS). (E) Cumulative distribution function of the ratio G_{Nap}/G_{Kdr} for the four clusters in A, showing the sequencing SS (gray) → RS (red) → ME (purple, 3 cells only) → PP (blue) predicted by the two-parameters bifurcation diagram in D. The wide PP range, as compared to SS and RS, merely comes from the fact that G_{Kdr} is small for cells in this cluster. The three colored points indicate the slopes of the oblique lines displayed in D (0.02, 0.12 and 0.48, respectively). (F) The data points in A are superimposed on the two-parameters bifurcation diagram shown in D, demonstrating a good agreement between our basic model and experimental data (the same color code as in A for the different clusters). The bifurcation diagram is simplified compared to A, only the region where repetitive spiking is possible (i.e. between the lines SN_1 and SN_2 in A) being displayed (shaded area). Notice that 3 ME cells (purple dots) are located close to the transition between the RS and PP regions. The four arrows indicate the presumable evolution of G_{Nap} and G_{Kdr} for SS, RS, ME and PP cells between E12.5 and E14.5-15.5. G_{Nap} eventually decreases while G_{Kdr} keeps on increasing. (G) Distribution of a sample of cells in the G_{Kdr} -

G_{Kdr} plane at E14.5. All the cells are located well within the SS region far from bifurcation lines because of the decreased G_{Nap} compared to E12.5, the increased G_{Kdr}, and the shift of the RS region (shaded) due to capacitance increase (18 versus 13 pF).

Figure 8. Effects of the slow inactivation of I_{Nap} on firing patterns predicted by computational modeling

(A) Examples of repetitive plateaus (left) and mixed events (right) recorded in $V1^R$ at E12.5 during a 2 s current pulse. (B1) Current-voltage curve of the basic model (without slow inactivation of I_{Nap}, and without I_A or channel noise) for G_{Kdr} = 5 nS and for G_{Nap} = 1.65 nS (lower curve) and 2 nS (upper curve). Solid lines denote stable fixed points and dashed lines unstable ones. For G_{Nap} =1.65 nS, bistability between quiescence and plateau occurs between 1.39 and 10.48 pA. When G_{Nap} is increased to 2 nS, the bistability region ranges from -10.84 to 9.70 pA, thus extending into the negative current range. This implies that once a plateau has been elicited, the model will stay in that stable state and not return to the resting state, even though current injection is switched off (see insert). B1 Insert. Voltage response to a 2 s current pulse of 15 pA for G_{Nap} = 2 nS. The resting state (gray dot on the lower curve in B1 is destabilized at pulse onset and a plateau is elicited (blue dot on the upper curve in B1). At pulse offset, the plateau is maintained, even though the injected current is brought back to zero, and channel noise is not sufficient to go back to the resting state. (B2) Domain of bistability between quiescence and plateau (shaded) in the I-G_{Nap} plane for G_{Kdr}= 5 nS. It is delimited by the line SN_2 where a SN bifurcation of fixed points occurs and by the subcritical Hopf bifurcation line HB where the plateau becomes unstable. Bistability requires that G_{Nap} exceeds 1.35 nS, and the domain of bistability enlarges as G_{Nap} is increased further. The two horizontal lines correspond to the two cases

shown in B1: G_{Nap} =1.65 nS and 2 nS. (C) Behavior of the model when slow inactivation is incorporated. The bifurcation diagram of the basic model (without slow inactivation) for I = 10 pA and G_{Kdr} = 5 nS (same conventions as in Fig 7B) and the stable limit cycle (black solid curve) obtained when slow inactivation is added are superimposed. The limit cycle is comprised of four successive phases (see labels): 1) long plateau during which I_{Nap} slowly inactivates, 2) fast transition to the quiescent state, 3) repolarization episode during which I_{Nap} slowly deinactivates, 4) fast transition back to the plateau. Each plateau starts with a full-blown action potential followed by rapidly decaying spikelets. Note that the bifurcation HB is subcritical here (unstable limit cycle shown by dashed red curve), at variance with square wave bursting (supercritical bifurcation and stable limit cycle); this is a characteristic feature of pseudo-plateau bursting. Note also that the plateau extends beyond the bifurcation HB because it is only weakly unstable then. Responses to a 15 s current pulse are shown on the right side. Top left: voltage response (G_{Nap}= 2.5 nS), Top right: behavior of the "effective" conductance of I_{Nap} channel, i.e., the maximal conductance G_{Nap} multiplied by the slow inactivation variable s. Bottom left: voltage trace when channel noise is added to fast and slow gating variables, Bottom right: Voltage trace when G_{Nap} is increased by 50% to 3.75 nS. (D) Mixed events. The bifurcation diagram of the basic model for G_{Kdr} = 5 nS and I = 12 pA and the stable limit cycle obtained in the presence of slow inactivation (G_{Nap} = 2.5 nS) are superimposed. Here again, the limit cycle is comprised of four successive phases (see labels): 1) slow inactivation of I_{Nap} that leads to the crossing of the bifurcation point HB_2 and then to the destabilization of the plateau potential, 2) fast transition to the spiking regime, 3) repetitive spiking during which I_{Nap} slowly de-inactivates, which leads to the crossing of the bifurcation point SN_2 and terminates the spiking episode, 4) fast transition back to the stable plateau potential. Response to a 15 s

current pulse of 12 pA is shown on the right in the absence of any channel noise. Top: Voltage trace (same labels as in the bifurcation diagram on the left), Bottom: Variations of the "effective" conductance $G_{Nap}s$ (same labels as in the voltage trace). Note that de-inactivation sufficient to trigger a new plateau occurs over a series of successive spikes, hence the small oscillations are visible on the trace. Note also that in C and D the first plateau lasts longer than the following ones, as in electrophysiological recordings of embryonic $V1^R$ cells displaying repetitive plateaus. This form of adaptation is caused by the slow inactivation of the persistent sodium current.

Supplementary legends

Figure 2—figure supplement 1. Effect of 4-AP on I_{Kdr} and I_A in embryonic V1^R

(A1) Example of voltage-dependent potassium currents evoked in response to 10 mV membrane potential steps (200 ms) from -100 mV or from -30 mV to +40 mV (10 s interval between pulses). V1^R were voltage clamped at V_H = -60 mV. A prepulse of -40 mV (300 ms) was applied to activate both I_A and I_{Kdr}. I_{Kdr} was evoked in response to 10 mV membrane potential steps (200 ms) from -100 mV to +40 mV. V1^R were voltage clamped at V_H = -60 mV. A prepulse of 30 mV (V_H = - 30 mV) was applied to isolate I_{Kdr}. (A1) Representative example of the effect of 300 µM 4-AP application on I_{Kdr} recorded from embryonic V1^R at E12.5. (B1) Curves showing current-voltage relationships of I_{Kdr} in control and in the presence of 300 µM 4-AP. Measurements were performed on traces shown in A1. (C1) Dose-response relationship of 4-AP-evoked I_{Kdr} inhibition (mean + SE). Data were normalized to I_{Kdr} amplitude measured in the absence of 4-AP (V_H = 40mV) and fitted as explained in Materials and Methods. Note that 4-AP IC_{50} is in µM range (2.9 µM). 0.3 µM 4-AP n = 3; N = 3, 1 µM 4-AP n = 3; N = 3, 3 µM 4-AP n = 9; N = 9, 10 µM 4-AP n = 13; N = 13, 30 µM 4-AP n = 7; N = 7, 100 µM 4-AP n = 7; N = 7, 300 µM 4-AP n = 7; N = 7. (A2) I_A was obtained as the difference between currents evoked from V_H = -100 mV and currents evoked from V_H = -30 mV (10 mV voltage step). (A2) Representative example of the effect of 300 µM 4-AP on I_A in V1^R recorded at E12.5. (B2) I_A Current-voltage ($I-V$) relationship in control conditions and in the presence of 300 µM 4-AP. The $I-V$ curves were obtained from the traces shown in A1. (C2) Bar graph showing the percentage of I_A block elicited by 4-AP. Note that 4-AP did not significantly block I_A (Wilcoxon test *P* = 0.065, n = 10).

Figure 2—figure supplement 2. Relates to Fig 2. Effect of 4-AP application in repetitively spiking $V1^R$ at E12.5

(A) Representative traces showing the effect of 4-AP application (300 μM) on Repetitive Spiking (RS) $V1^R$ at E12.5. Note that plateau potential activity evoked in the presence of 4-AP (middle trace) was blocked by 0.5 μM TTX (right trace). (B) Bar plots showing the changes in the firing pattern of RS $V1^R$ evoked by 300 μM 4-AP application (n = 14). 4-AP application evoked a plateau potential in 71.4 % of the recorded neurons (10/14) and mixed events in 14.3% of the recorded neurons (2/14). The excitability pattern was not modified in 2 neurons. Repetitive Spiking (RS) $V1^R$ (red), Mixed events (ME) $V1^R$ (purple), Plateau Potential (PP) $V1^R$ (blue).

Figure 3—figure supplement 1. Distributions of log ½Ad, CV ½Ad and log ddr values related to the cluster analysis of embryonic $V1^R$ firing patterns

(A1) Histogram of log mean ½Ad (mean half amplitude event duration) for the whole $V1^R$ population at E12.5 (n= 164; bin width 0.1). The histogram was well fitted by the sum of three Gaussian curves with means and SDs of 1.135, 2.046 & 2.84, and 0.316, 0.181 & 0.21, respectively. (A2) Histogram of the values of log mean ½Ad sorted after cluster analysis showing single spiking (SS) $V1^R$ (gray), repetitive spiking (RS) $V1^R$ (red), mixed events (ME) $V1^R$ with short plateau potentials (ME short PP $V1^R$, light purple), ME $V1^R$ with long plateau potentials (ME long PP $V1^R$, dark purple) and plateau potential (PP) $V1^R$ (blue). log mean ½Ad was significantly different between SS $V1^R$, PP $V1^R$, the whole ME $V1^R$ population (ME_s and ME_l $V1^R$) and PP $V1^R$ (Kruskall-Wallis test $P < 0.0001$; SS $V1^R$ versus RS $V1^R$, $P < 0.0001$; SS $V1^R$ versus ME $V1^R$, $P < 0.0001$; SS $V1^R$ versus PP $V1^R$, $P < 0.0001$; RS $V1^R$ versus ME $V1^R$, $P = 0.0004$; RS $V1^R$ versus PP $V1^R$, $P < 0.0001$; ME $V1^R$ versus PP $V1^R$, $P = 0.018$; SS $V1^R$ n = 46,

RS $V1^R$ n = 69, ME_s $V1^R$ n = 9, ME_l $V1^R$ n = 4, PP $V1^R$ n = 35). (B1) Histogram of CV ½Ad for the whole $V1^R$ population at E12.5 (n= 164; bin width 5%). Note that a large population of $V1^R$ had zero CV ½Ad (n = 83). The histogram for CV ½Ad ≠ 0 was fitted by the sum of three Gaussian curves with means and SDs of 23.4, 68.4 & 117 (%) and 8.9, 6.8 & 4.1, respectively. (B2) Histograms of the values of CV ½Ad sorted after cluster analysis showing SS $V1^R$ (black), RS $V1^R$ (red), ME_s $V1^R$ (light purple), ME_l $V1^R$ (dark purple) and PP $V1^R$. CV ½Ad was not significantly different between SS $V1^R$ and PP $V1^R$ (CV ½Ad of SS $V1^R$ and PP $V1^R$ = 0.682 % and 0% respectively: only one of the 46 SS $V1^R$ displayed 3 PA and had a CV ½Ad of 31.37). CV ½Ad was significantly different between RS $V1^R$ and the whole ME $V1^R$ population and also between SS $V1^R$ or PP $V1^R$ and RS $V1^R$ or ME $V1^R$ (Kruskall-Wallis test $P < 0.0001$; SS $V1^R$ versus RS $V1^R$ $P < 0.0001$, SS $V1^R$ versus ME $V1^R$ $P < 0.0001$, SS $V1^R$ versus PP $V1^R$ $P = 0.846$, RS $V1^R$ versus ME $V1^R$ $P = 0.0003$, RS $V1^R$ versus PP $V1^R$ $P < 0.0001$, ME $V1^R$ versus PP $V1^R$ $P < 0.0001$). (C1) Histogram of log ddr (sum of ½Ad divided by pulse duration) for the whole $V1^R$ population at E12.5 (n= 164; bin width 0.2). The histogram was fitted by the sum of two Gaussian curves with means and SDs of -2.51 & -0.851, and 0.2 & 0.46, respectively. (C2) Histograms of the values of log ddr sorted after cluster analysis showing SS $V1^R$ (black), RS $V1^R$ (red), ME_s $V1^R$ (light purple), ME_l $V1^R$ (dark purple) and PP $V1^R$. log (ddr) was not significantly different between ME $V1^R$ and PP $V1^R$, while it was significantly different between SS $V1^R$ and RS $V1^R$, SS $V1^R$ and the whole ME $V1^R$ population, SS $V1^R$ and PP $V1^R$, RS $V1^R$ and the whole ME $V1^R$ population, RS $V1^R$ and PP $V1^R$ (Kruskall-Wallis test $P < 0.0001$; SS $V1^R$ versus RS $V1^R$, $P < 0.0001$; SS $V1^R$ versus ME $V1^R$, $P < 0.0001$; SS $V1^R$ versus PP $V1^R$, $P < 0.0001$; RS $V1^R$ versus ME $V1^R$, $P < 0.0001$; RS $V1^R$ versus PP $V1^R$, $P < 0.0001$; ME $V1^R$ versus PP $V1^R$, $P = 0.977$). ME_s $V1^R$ and ME_l $V1^R$ differed only by their CV ½Ad (Mann-Whitney test, log mean ½Ad for ME_s $V1^R$ versus log mean ½Ad for ME_l $V1^R$, $P = 0.26$; CV

½Ad for ME_s $V1^R$ versus CV ½Ad ME_I $V1^R$, *P* = 0.0028 and log ddr for ME_s $V1^R$ versus log ddr for ME_I $V1^R$, *P* = 0.1483). It is noteworthy that the distribution of the values of each metric was multimodal thus indicating that each of them could partially discriminate different groups of embryonic $V1^R$ according to their firing pattern.

Figure 6—figure supplement 1. I_{Nap} is present in embryonic $V1^R$ recorded at E14.5

(A) Representative trace of I_{Nap} evoked by a slow depolarizing voltage ramp (70 mV/s, upper insert) in SS embryonic $V1^R$ (lower insert). I_{Nap} was isolated by subtracting currents evoked by depolarizing ramps in the presence of 1 μM TTX to the control current evoked in the absence of TTX (upper insert). (B) Voltage dependence of G_{Nap} conductance calculated from the trace shown in A. The activation curve was obtained by transforming the current evoked by a depolarizing voltage ramp from -100 mV to 20 mV (70 mV/s) using the following equation: $G_{NaP} = -I_{Nap}/((-Vh)+E_{Na})$ where Vh is the holding potential at time t during a depolarizing voltage ramp and E_{Na} is the equilibrium potential for sodium (E_{Na} = 60 mV). The G_{NaP}/Vh curve was fitted with the following Boltzmann function: $G = G_{MAX}/(1+\exp(-(V-V_{HALF})/k))$ (Boeri et al. 2018), where V_{half} is the Vh value for G_{Nap} half activation, k the slope factor of the curve and G_{max} the maximum conductance. We found no significant difference between the values of V_{half} (Mann-Whitney test: *P* = 0.8518) and of k (Mann-Whitney test: *P* = 0.7546) obtained at E12.5 (Boeri et al. 2018) and those obtained at E14.5. At E14.5 V_{half} = -27 ± 5.1 mV and k = 7.73 ± 0.78 (n = 6).

Figure 6—figure supplement 2. I_{Kdr} was inhibited by 4-AP in $V1^R$ recorded at E14.5

(A1) Representative examples of the total outward K^+ currents obtained from V_H = -100 mV (left traces), of I_{Kdr} (V_H = -30 mV, middle traces) and of isolated I_A (left traces) recorded in

single spiking (SS) $V1^R$ at E14.5. (A2) Current-voltage relationship of I_{Kdr} (filled circle) and of I_A (open circle) in SS $V1^R$ at E14.5. $I-V$ curves were obtained from currents shown in A1. (B1) Representative example of the effect of 4-AP at 600 µM in $V1^R$ at E14.5. (B2) Current-voltage curves in control condition and in the presence of 600 µM 4-AP. (B3) Bar plots showing the percentage of I_{Kdr} inhibition evoked by 300 µM 4-AP application (n = 8) and by 600 µM 4-AP application (n = 7). The percentages of I_{Kdr} inhibition evoked by 300 µM 4-AP and by 600 µM 4-AP applications were not significantly different (*P* = 0.574). (C1) Representative example of the effect of 600 µM 4-AP on I_A in $V1^R$ recorded at E14.5. (C2) $I-V$ curves in control conditions and in the presence of 600 µM 4-AP. These curves were obtained from the traces shown in B1. (C3) Bar graph showing the percentage of I_A block elicited by 4-AP. 4-AP did not significantly block I_A (Wilcoxon test *P* = 0.11, n = 6).

Figure 7—figure supplement 1. Effects of I_A on embryonic $V1^R$ firing patterns predicted by computational modeling

(A) The maximal conductances of I_{Kdr} and I_A at E12.5 are linearly correlated. Best fit: G_A = 1.09 G_{Kdr} (R^2 = 0.81, N=44). (B) Effect of I_A on the dynamics of the basic model. The one-parameter bifurcation diagrams in control condition (black, I = 20 pA, G_{Kdr} = 10 nS, no I_A, same as in Fig 7B) and with I_A added (orange, G_A = 10 nS) are superimposed. The I_A current shifts the firing threshold SN_1 to the right by 0.18 nS (see also C) as indicated by the orange arrow, with little effect on the amplitude of action potentials (see also insert in C). In contrast, I_A shifts SN_2 by only 0.03 nS because it is inactivated by depolarization. (C) I_A also slows down the discharge frequency, as shown by comparing the $G_{Nap}-V$ curves without I_A (black) and with I_A (orange). For G_{Nap} = 1 nS, for instance, the firing frequency is reduced by 31%, from 15 to 10.4 Hz. Here again, the effect of I_A progressively decreases as

1511 G_{Nap} increases because of the membrane depolarization elicited by I_{Nap}. For G_{Nap} = 2.4 nS,
1512 for instance, the firing frequency is reduced by 11% only, from 19.1 to 17 Hz. This
1513 frequency reduction elicited by I_A does not merely result from the increased firing
1514 threshold. Note also that the latency of the first spike is increased (see voltage trace in
1515 insert), which is a classical effect of I_A. (D) I_A reduces the frequency of pseudo-plateau
1516 bursting by lengthening quiescent episodes (doubling their duration in the example shown)
1517 without affecting the duration of plateaus much (here a mere 5% increase), as shown by
1518 the comparison of the voltage traces obtained without I_A (control, $G_{Kdr} = 2.5$ nS, black)
1519 and with I_A ($G_{Kdr} = G_A = 2.5$ nS, orange). This is because I_A is activated near rest but
1520 inactivated during voltage plateaus. Note that increasing G_{Kdr}, in the absence of I_A has not
1521 the same effect; it shortens both plateaus and quiescent episodes (see Fig 8C, where
1522 $G_{Kdr} = 5$ nS). Again, this is because I_{Kdr} does not inactivate (or does it only very slowly), in
1523 contrast to I_A.
1524
1525 **Figure 7—figure supplement 2. Explaining the effect of 4-AP on the firing pattern**
1526 The RS region of the basic model, where repetitive firing may occur, is displayed in the
1527 $G_{Nap} - G_{Kdr}$ plane in control condition for E12.5 V1^R (C_{in} = 13 pF, G_{in} = 1 nS, I = 20 pA,
1528 shaded area), and when G_{in} and I were both reduced by 25% (middle curve) or by 50% (left
1529 curve). The reduced I accounts for the decrease in rheobase, and thus in the current
1530 injected in the experiments, following the decrease in G_{in}. If 4-AP reduced only G_{Kdr} (as
1531 indicated by the downward arrow) the firing pattern of SS V1^R would not change, the RS
1532 region being too far to the right to be visited. In contrast, when the effects of 4-AP on the
1533 input conductance and rheobase are taken into account, the bifurcation diagram moves
1534 leftwards and downwards, as indicated by the oblique black arrow, and the RS and PP

regions are then successively entered as G_{Kdr} is reduced. The same explanation holds at E14.5.

Figure 3-souce data-1

Numerical data used to perform cluster analysis shown in Figure 3

TABLE 1 Model parameters

Parameter	Basic model	Model with slow inactivation of I_{Nap}
Passive parameters		
Input conductance G_{in}	1 nS	same
Input capacitance C_{in}	13 pF (E12.5, Figs. 7B, C, D and F and 8B to D) or 18 pF (E14.5, Fig. 7G)	13 pF
Resting potential V_r	-60 mV	same
Injected current I	20 pA (Fig. 7B to G)	10 pA (Fig. 8C) or 12 pA (Fig. 8D) variable in Fig. 8B
Transient sodium current I_{nat}		
Maximal conductance G_{Nat}	20 nS	same
Reversal potential E_{Na}	60 mV	
Activation exponent	3	
Mid-activation V_m	-26 mV	
Steepness of activation k_m	9.5 mV	
Activation time constant	1.5 ms	
Mid-inactivation V_h	-45 mV	
Steepness of inactivation K_h	-5 mV	
Inactivation time constant τ_m	Voltage-dependent (see Material and Methods)	
Persistent sodium current I_{Nap}		
Maximal conductance	variable (see text and figure captions)	same
Mid-activation voltage	-36 mV	same
Mid-inactivation V_s		-30 mV
Steepness of inactivation k_s		-5 mV
Inactivation time constant	Slow inactivation not included	2 s
Delayed rectifier potassium current I_{Kdr}		
Maximal conductance G_{Kdr}	variable (see text and figure captions)	same
Reversal potential E_K	-96 mV	
Activation exponent	3	
Mid-activation V_n	-20 mV	
Steepness of activation k_n	15 mV	
Activation time constant τ_m	10 ms	
Potassium A current I_A (when included in the basic model)		
Maximal conductance G_A	Equal to G_{Kdr}	never included
Mid-activation V_{mA}	-30 mV	
Steepness of activation k_{mA}	12 mV	
Activation time constant	Instantaneous activation	
Mid-inactivation V_{hA}	-70 mV	

Steepness of inactivation k_{hA}	-7 mV	
Inactivation time constant τ_{hA}	23 ms	

1542
1543

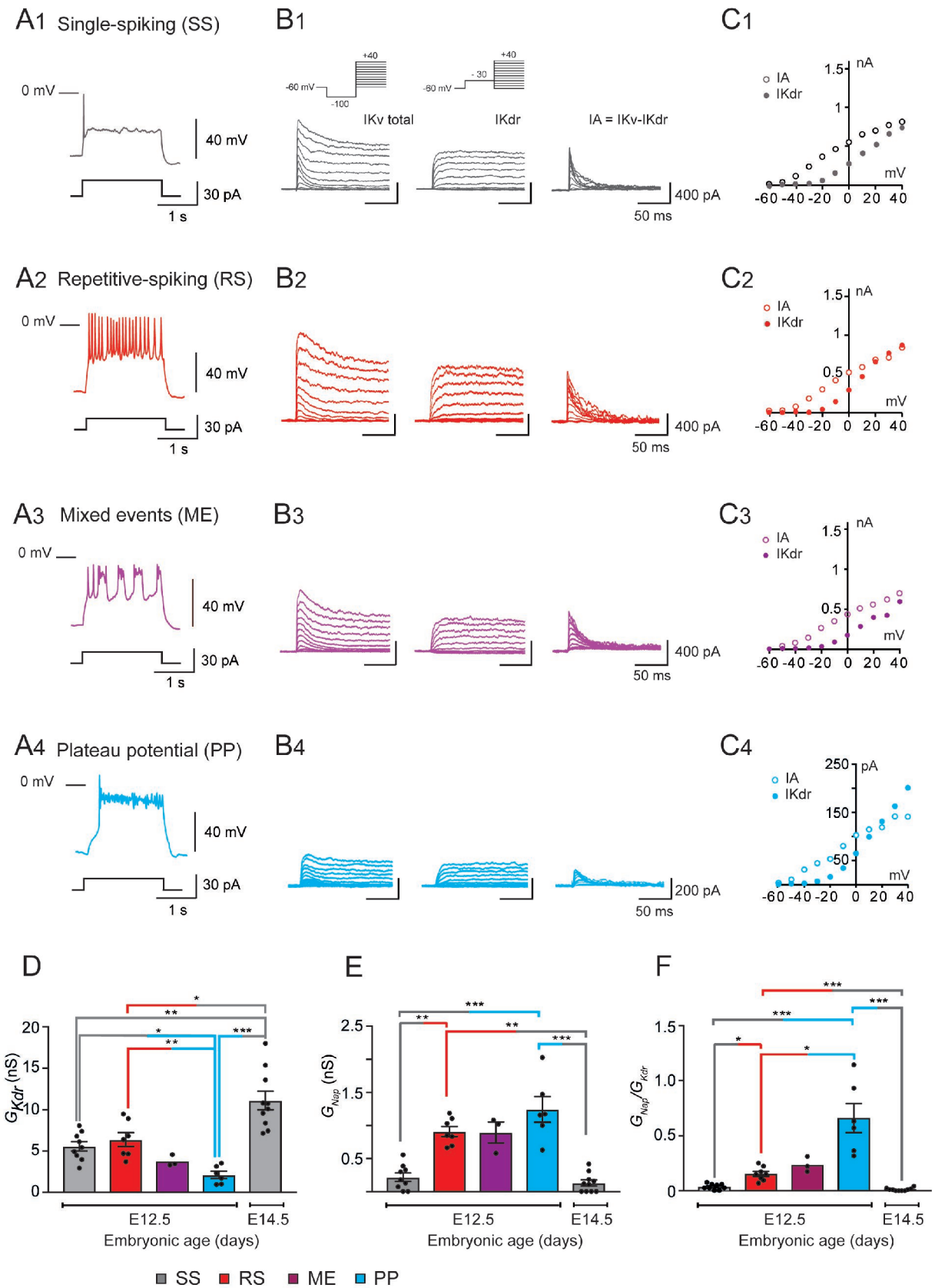
A1 Single-spiking (SS)
B1
C1
0 mV
40 mV
30 pA
1 s
+40
-60 mV
-100
- 30
IKv total
IKdr
IA = IKv-IKdr
400 pA
50 ms
IA
IKdr
nA
mV
A2 Repetitive-spiking (RS)
B2
C2
A3 Mixed events (ME)
B3
C3
A4 Plateau potential (PP)
B4
C4
200 pA
pA
D
E
F
G_{Kdr} (nS)
G_{Nap} (nS)
G_{Nap}/G_{Kdr}
E12.5
E14.5
Embryonic age (days)
SS
RS
ME
PP

Fig 1

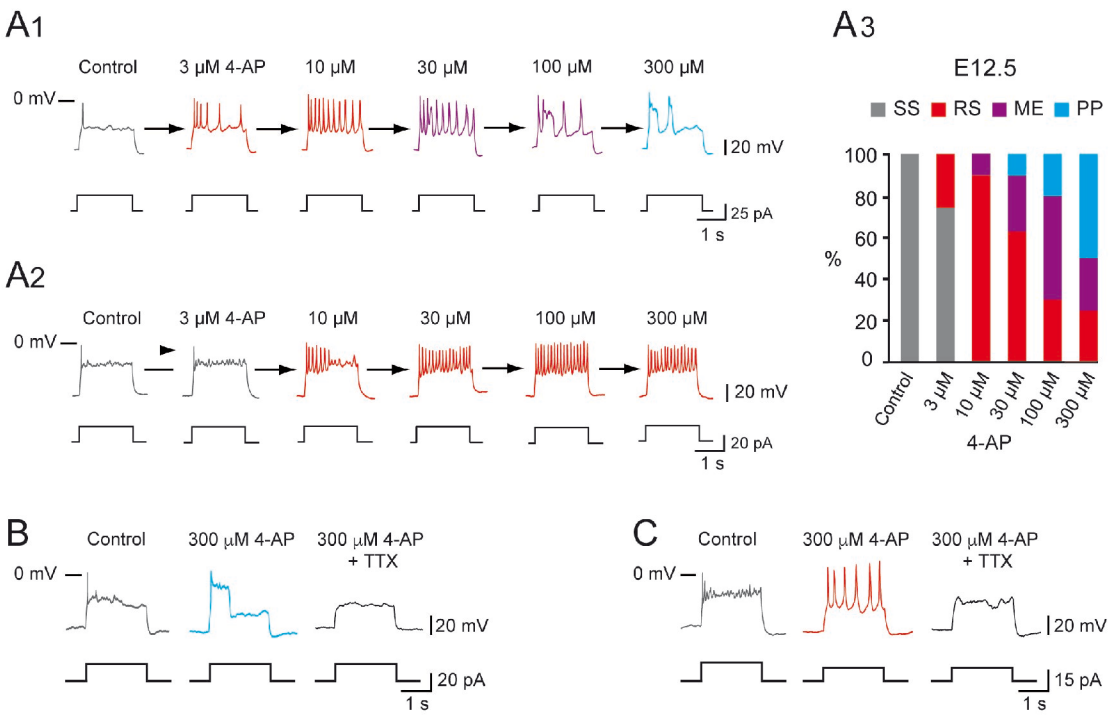
A1
Control
3 μM 4-AP
10 μM
30 μM
100 μM
300 μM
0 mV
20 mV
25 pA
1 s
A2
Control
3 μM 4-AP
10 μM
30 μM
100 μM
300 μM
0 mV
20 mV
20 pA
1 s
A3
E12.5
SS
RS
ME
PP
100
80
60
40
20
0
%
Control
3 μM
10 μM
30 μM
100 μM
300 μM
4-AP
B
Control
300 μM 4-AP
300 μM 4-AP
+ TTX
0 mV
20 mV
20 pA
1 s
C
Control
300 μM 4-AP
300 μM 4-AP
+ TTX
0 mV
20 mV
15 pA
1 s

Fig 2

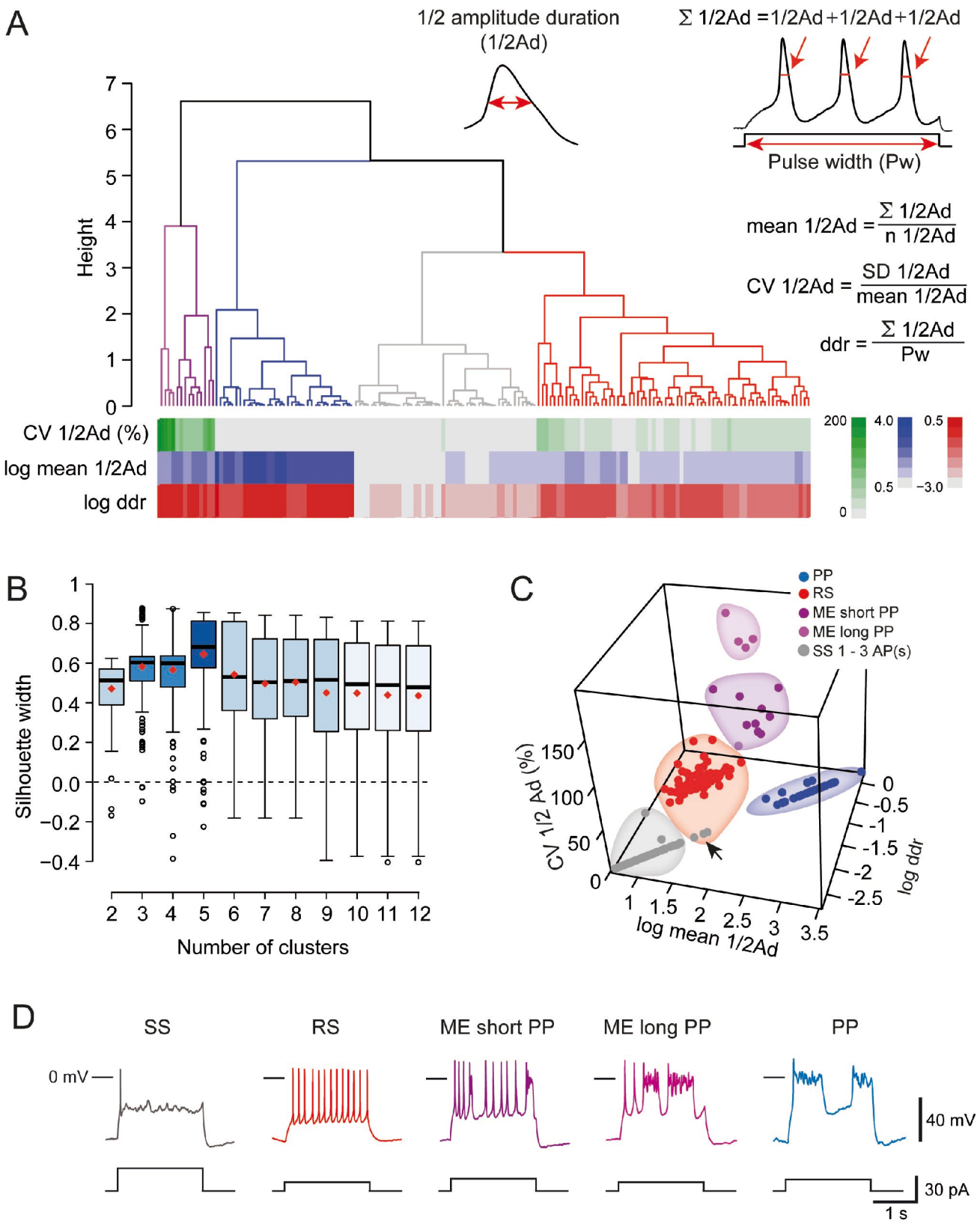
A
1/2 amplitude duration
(1/2Ad)
Σ 1/2Ad =1/2Ad+1/2Ad+1/2Ad
Pulse width (Pw)
mean 1/2Ad = Σ 1/2Ad / n 1/2Ad
CV 1/2Ad = SD 1/2Ad / mean 1/2Ad
ddr = Σ 1/2Ad / Pw
Height
CV 1/2Ad (%)
log mean 1/2Ad
log ddr
B
Silhouette width
Number of clusters
C
PP
RS
ME short PP
ME long PP
SS 1 - 3 AP(s)
CV 1/2 Ad (%)
log mean 1/2Ad
log ddr
D
SS
RS
ME short PP
ME long PP
PP
0 mV
40 mV
30 pA
1 s

Fig 3

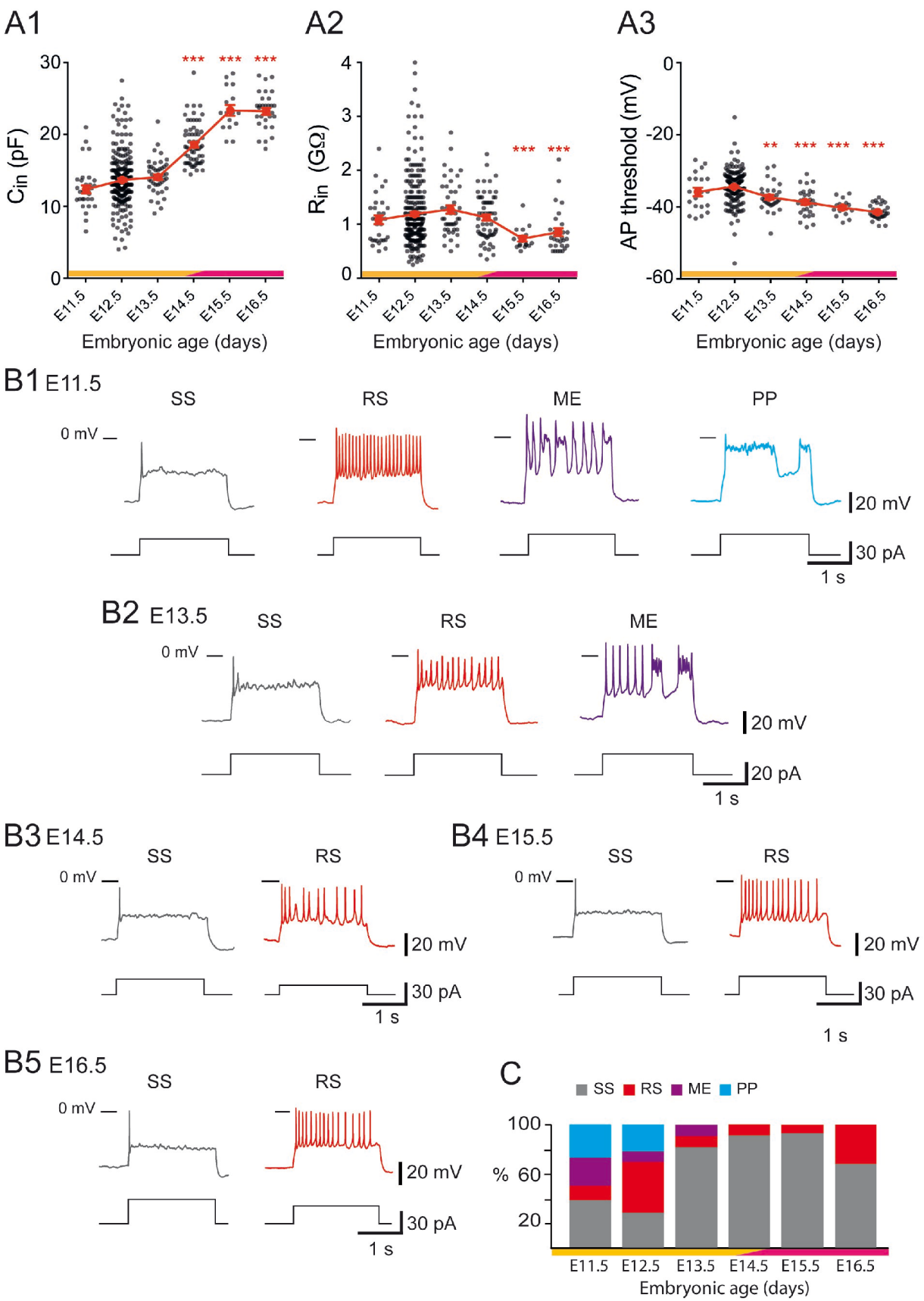
A1
A2
A3
C_{in} (pF)
R_{in} (GΩ)
AP threshold (mV)
E11.5
E12.5
E13.5
E14.5
E15.5
E16.5
Embryonic age (days)
B1 E11.5
SS
RS
ME
PP
0 mV
20 mV
30 pA
1 s
B2 E13.5
B3 E14.5
B4 E15.5
B5 E16.5
C
% 60
100
20

Fig 4

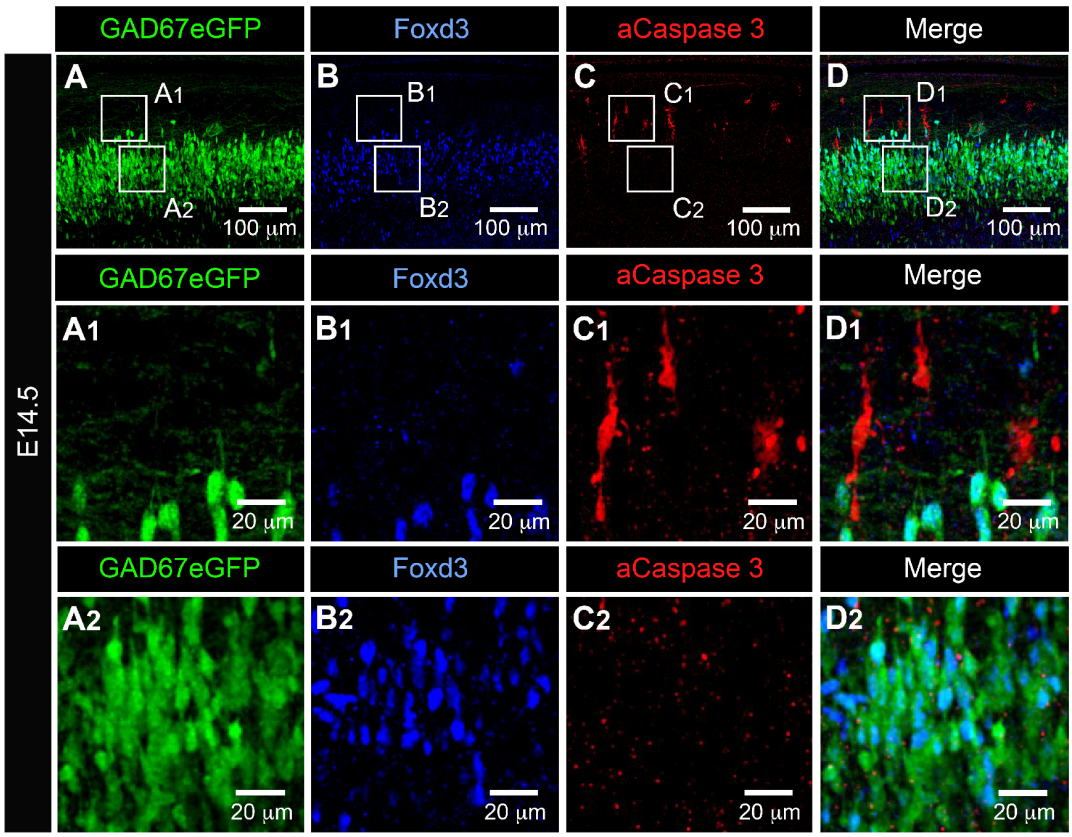
GAD67eGFP
Foxd3
aCaspase 3
Merge
A
A1
A2
B
B1
B2
C
C1
C2
D
D1
D2
100 μm
E14.5
20 μm

Fig 5

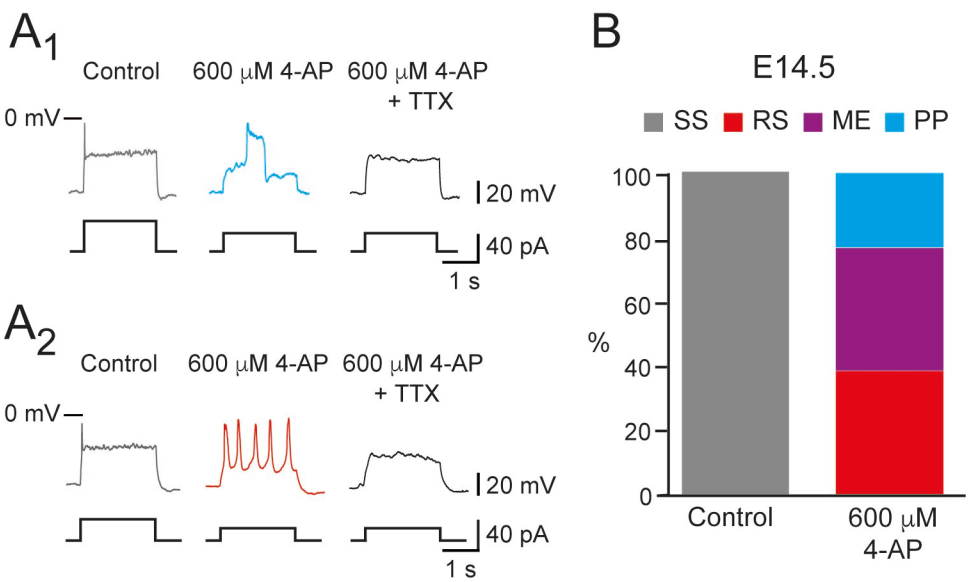
A1
Control
600 μM 4-AP
600 μM 4-AP
+ TTX
0 mV
20 mV
40 pA
1 s
A2
Control
600 μM 4-AP
600 μM 4-AP
+ TTX
0 mV
20 mV
40 pA
1 s
B
E14.5
SS
RS
ME
PP
100
80
60
40
20
0
%
Control
600 μM
4-AP

Fig 6

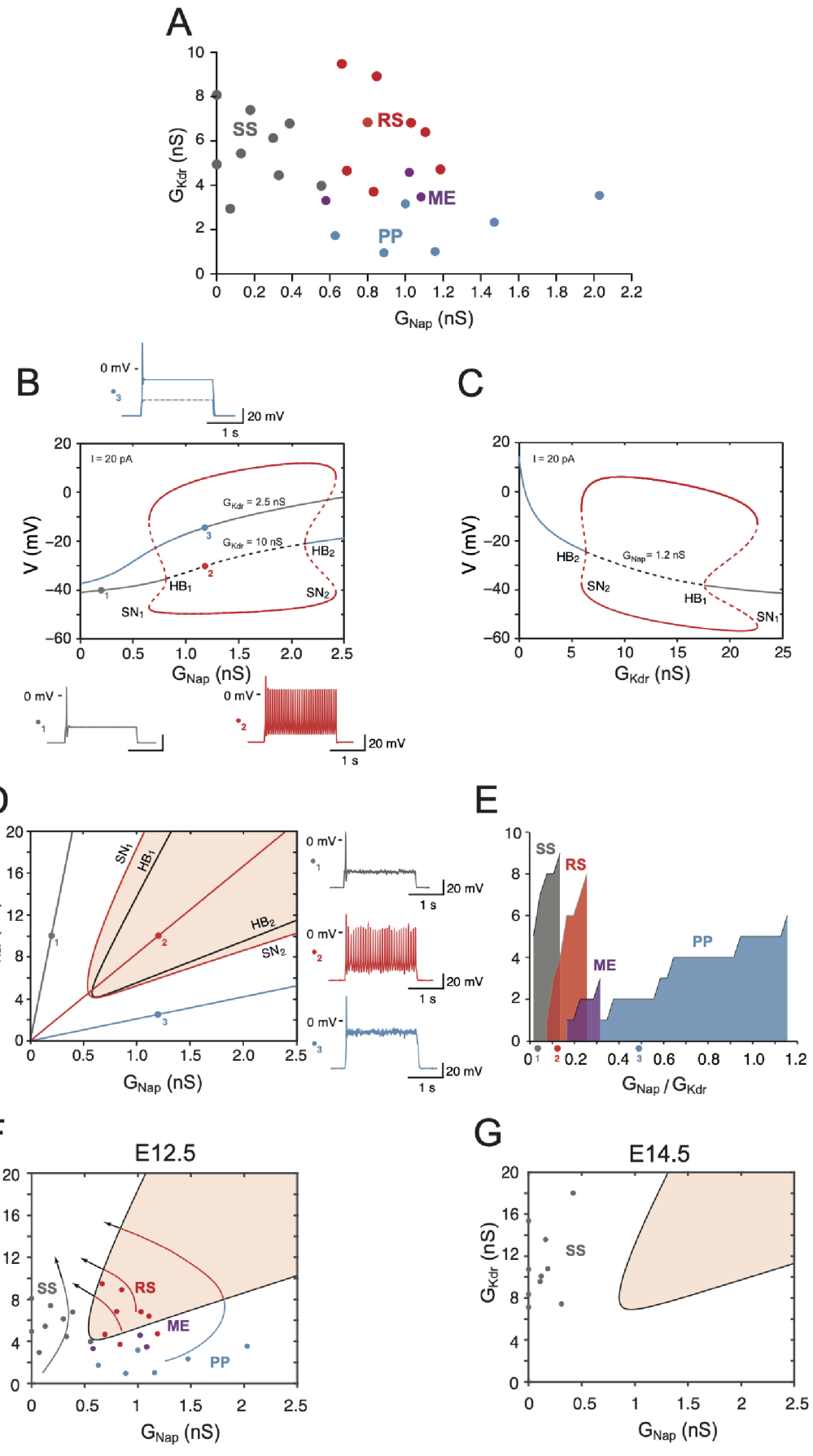
A
SS
RS
ME
PP
G_Kdr (nS)
G_Nap (nS)
B
0 mV
20 mV
1 s
I = 20 pA
G_Kdr = 2.5 nS
G_Kdr = 10 nS
HB1
HB2
SN1
SN2
V (mV)
G_Nap (nS)
C
I = 20 pA
G_Nap = 1.2 nS
G_Kdr (nS)
D
E
G_Nap / G_Kdr
F
E12.5
G
E14.5

Fig 7

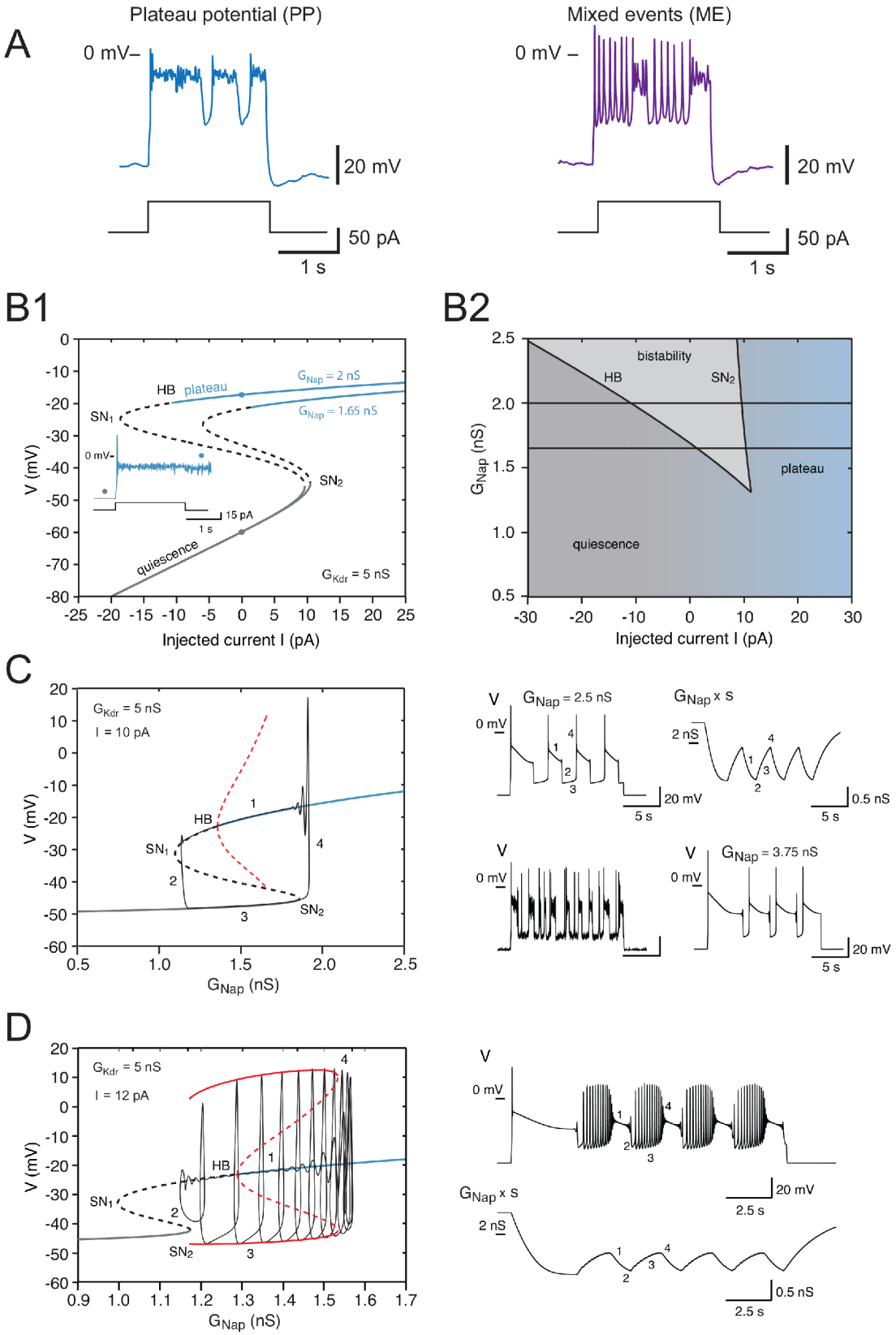
A
Plateau potential (PP)
0 mV
20 mV
50 pA
1 s
Mixed events (ME)
0 mV
20 mV
50 pA
1 s
B1
HB
plateau
G_{Nap} = 2 nS
G_{Nap} = 1.65 nS
SN_1
SN_2
0 mV
15 pA
1 s
quiescence
G_{Kdr} = 5 nS
V (mV)
Injected current I (pA)
B2
bistability
HB
SN_2
plateau
quiescence
G_{Nap} (nS)
Injected current I (pA)
C
G_{Kdr} = 5 nS
I = 10 pA
HB
SN_1
SN_2
V (mV)
G_{Nap} (nS)
V
G_{Nap} = 2.5 nS
0 mV
20 mV
5 s
G_{Nap} x s
2 nS
0.5 nS
5 s
V
0 mV
V
G_{Nap} = 3.75 nS
0 mV
20 mV
5 s
D
G_{Kdr} = 5 nS
I = 12 pA
HB
SN_1
SN_2
V (mV)
G_{Nap} (nS)
V
0 mV
20 mV
2.5 s
G_{Nap} x s
2 nS
0.5 nS
2.5 s

Fig 8

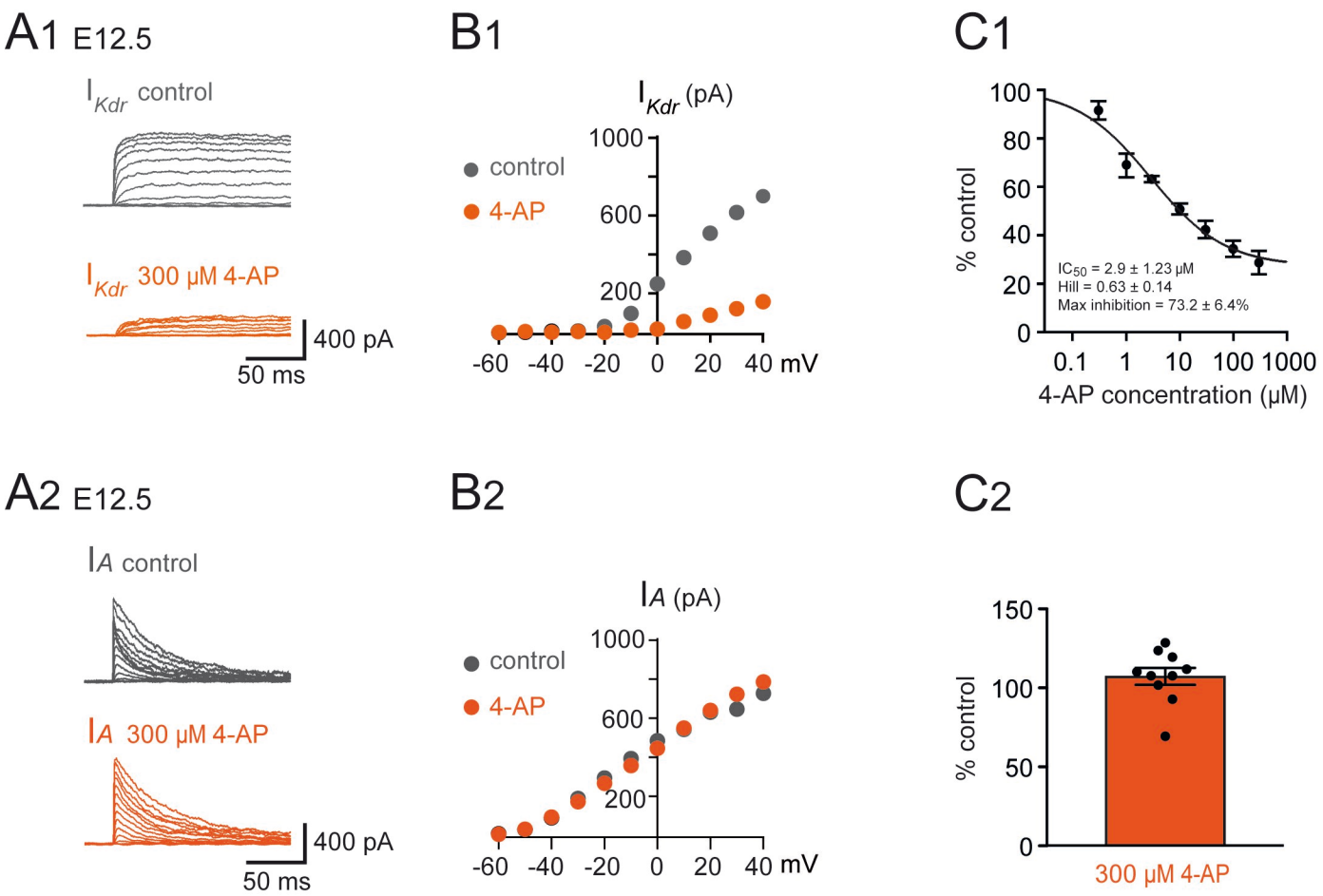

Fig 2 figure supplement 1

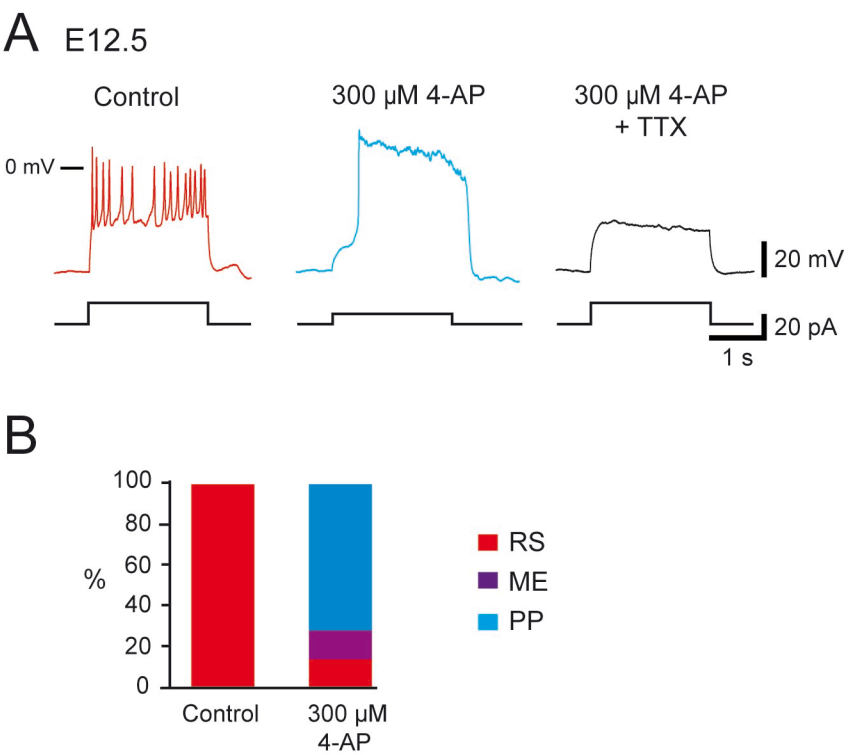

Fig 2 figure supplement 2

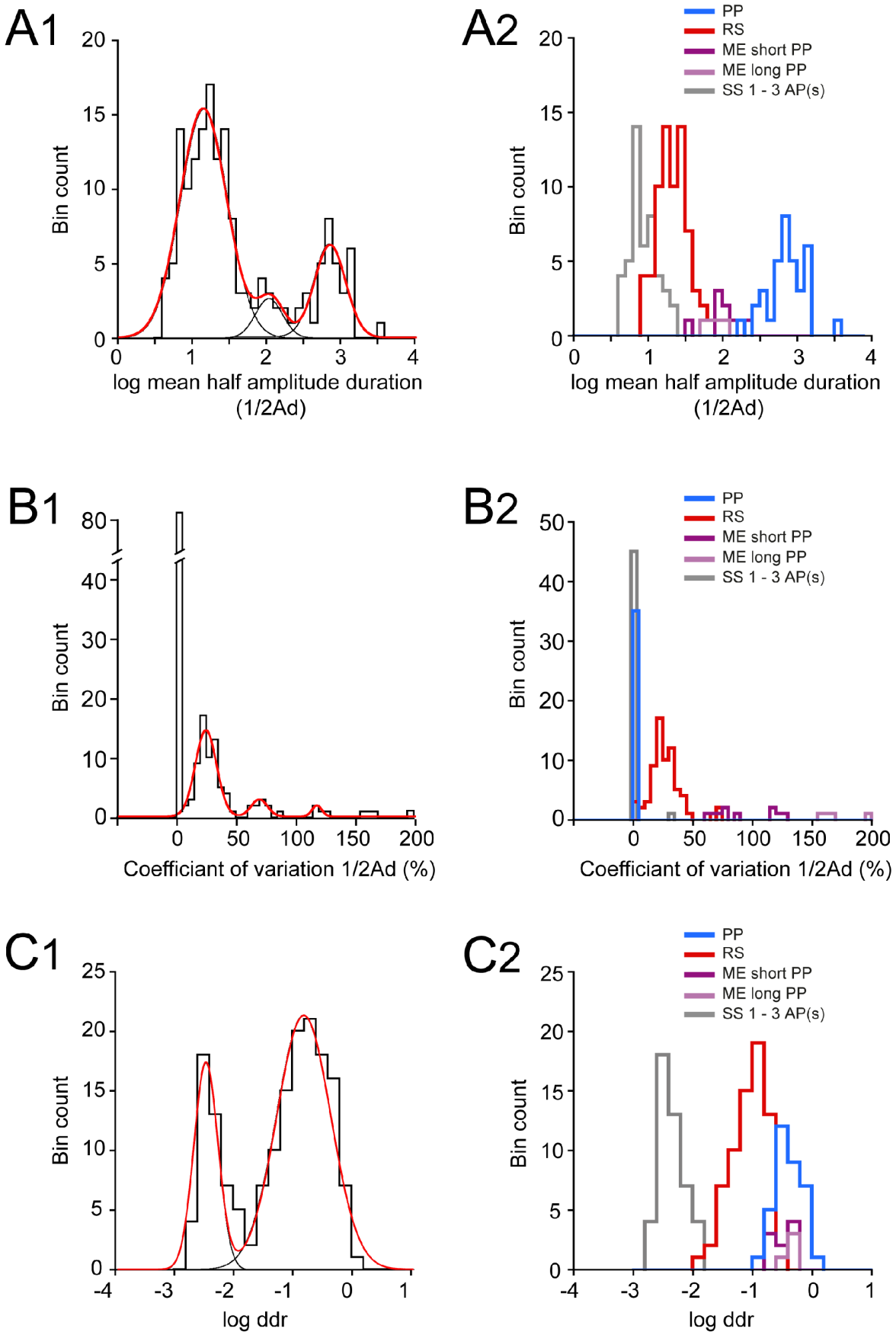

Fig 3 figure supplement 1

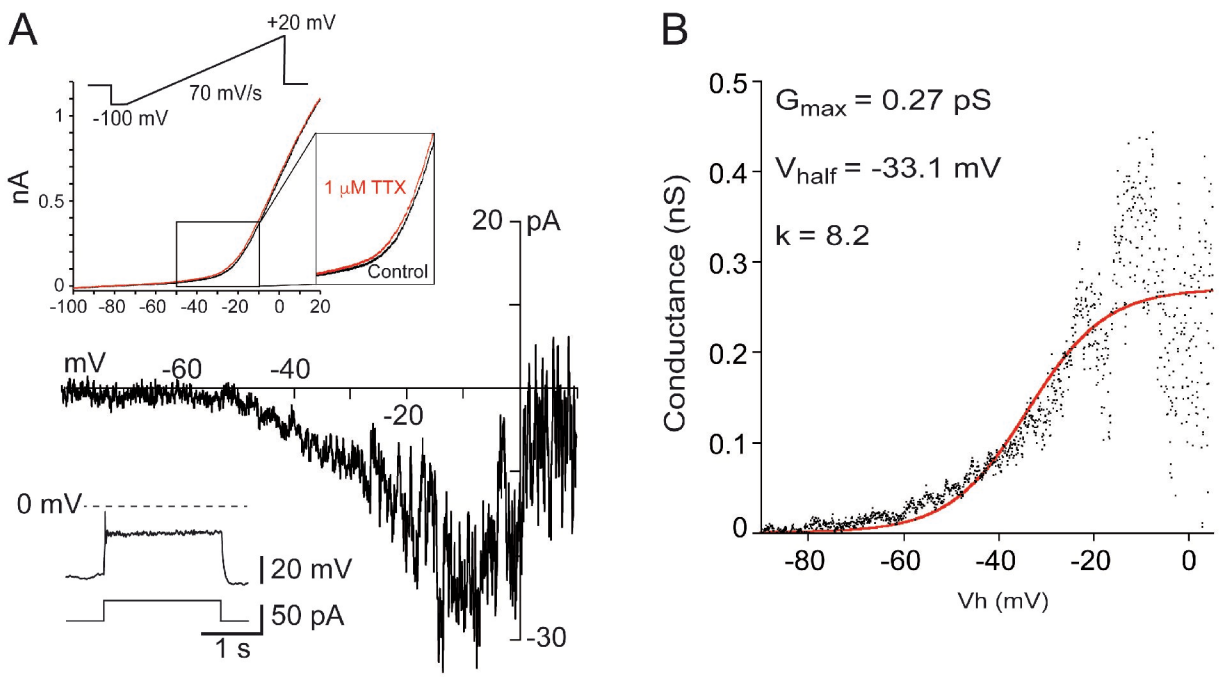

Fig 6 figure supplement 1

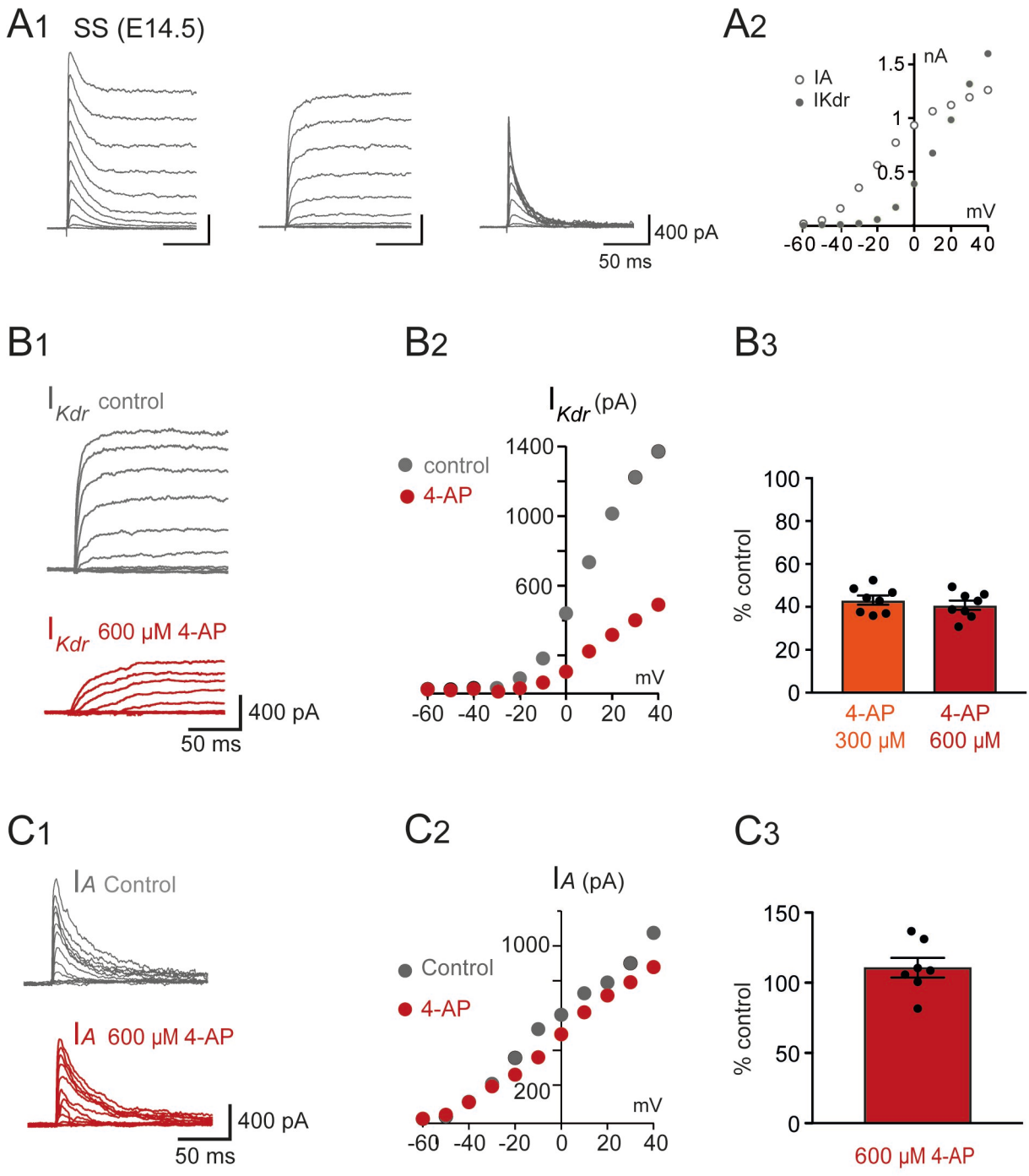

Fig 6 figure supplement 2

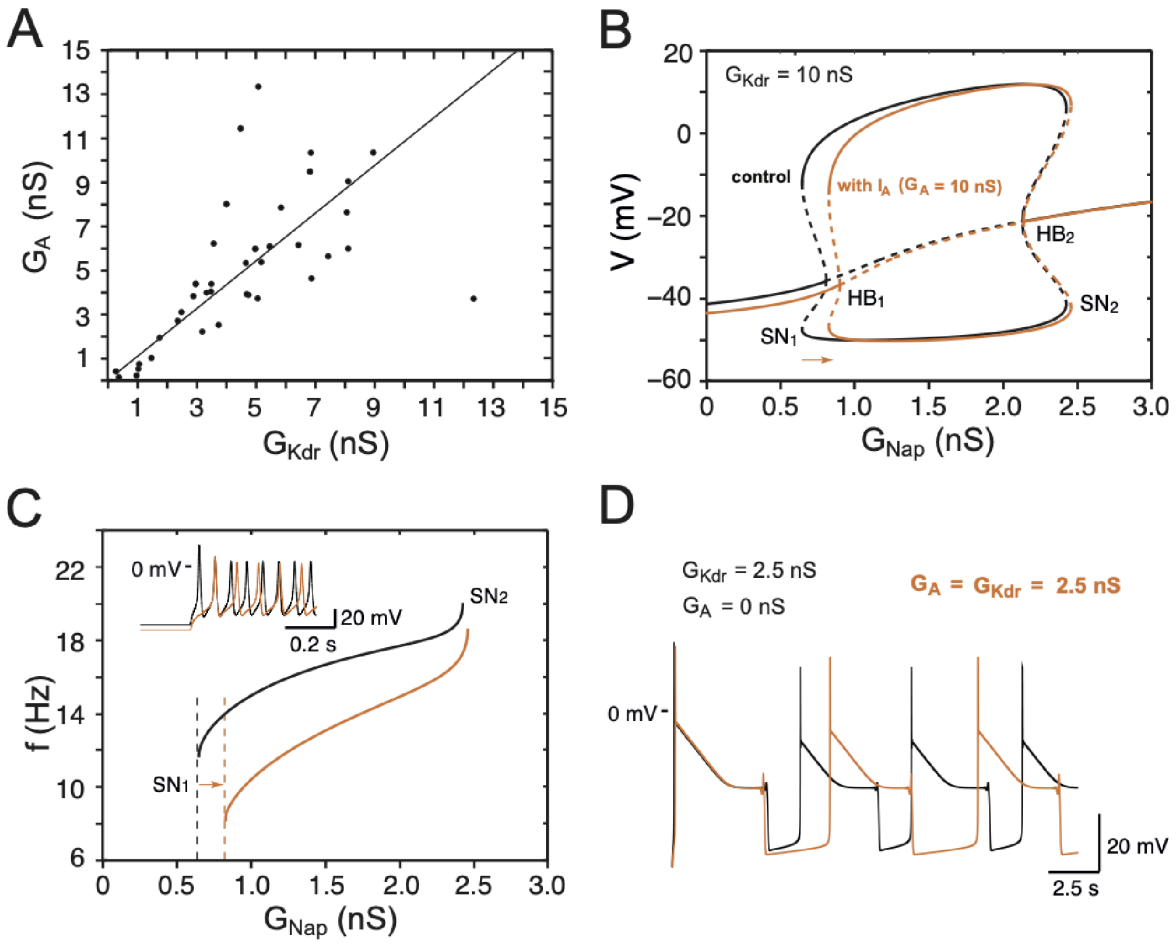

Fig 7 figure supplement 1

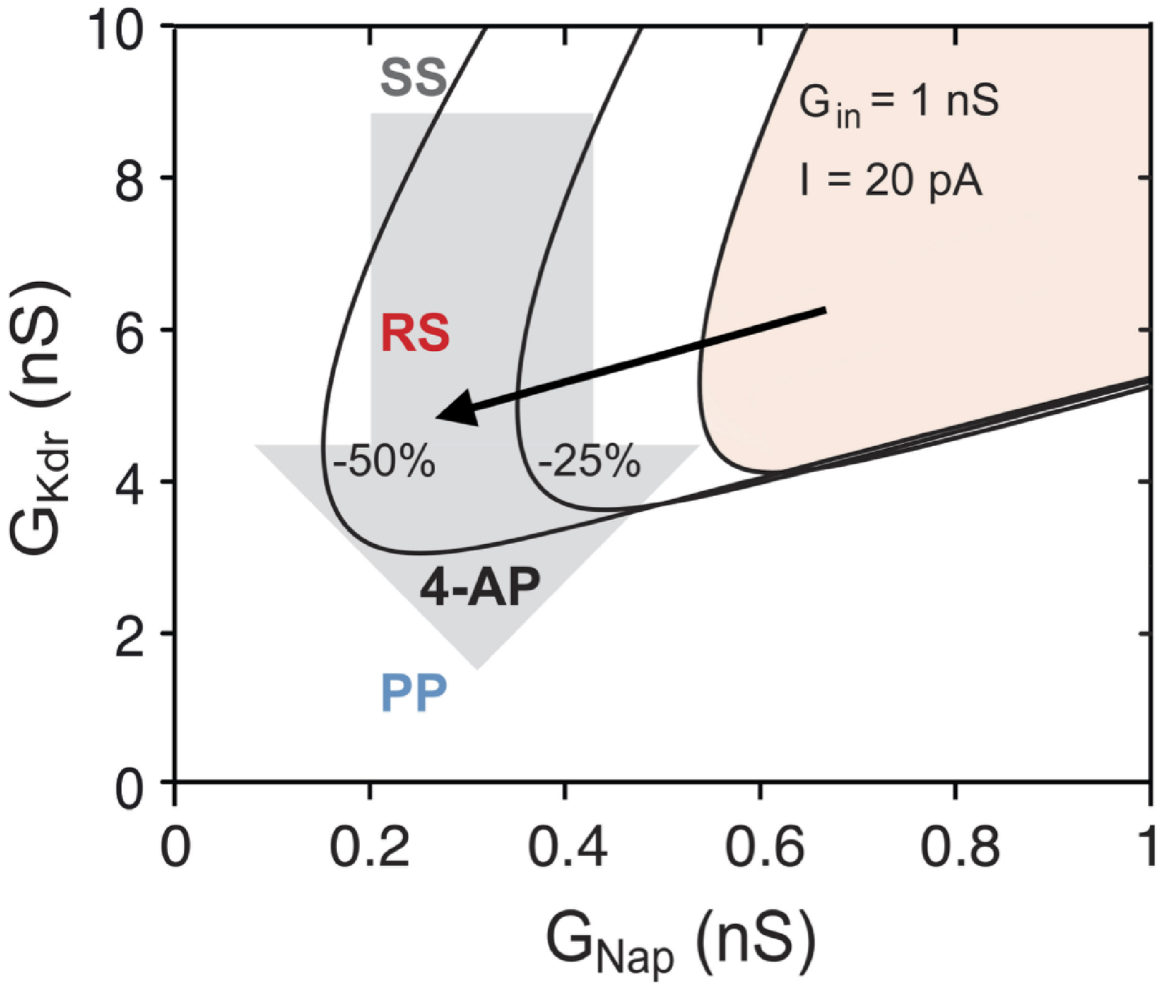

Fig 7 figure supplement 2